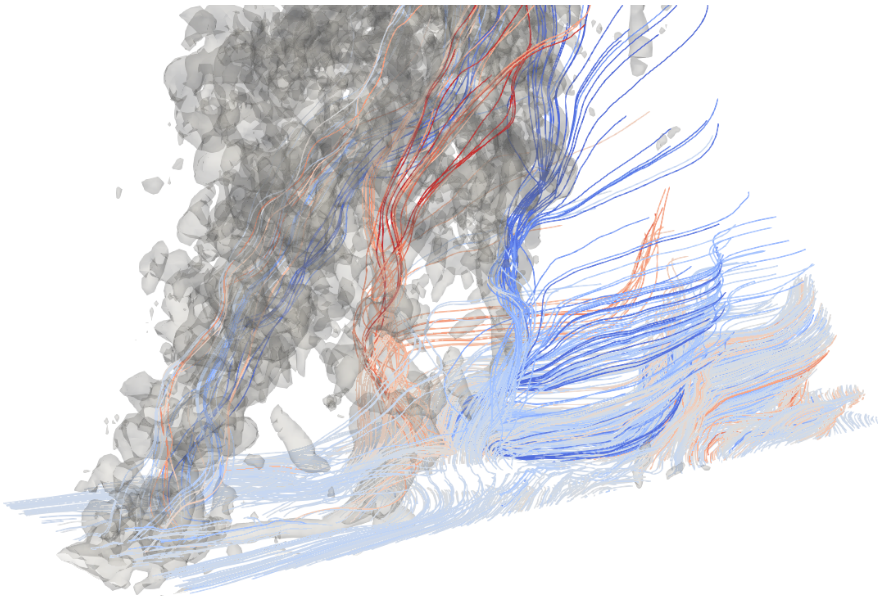

The Influence of Uncertainty Factors in Modeling the Smoke Plume Rise in the Surface Atmospheric Layer

Ricardo Daniel Cardona de Sousa Bento

Thesis to obtain the Master of Science Degree in

Mechanical Engineering

Supervisors: Prof. José Carlos Fernandes Pereira
Eng. Francisco de Lemos Cabral Granadeiro Martins

Examination Committee

Chairperson: Prof. José Manuel da Silva Chaves Ribeiro Pereira
Supervisor: Prof. José Carlos Fernandes Pereira
Member of the Committee: Prof. Miguel Abreu de Almeida Mendes

July 2024

Declaration

I declare that this document is an original work of my own authorship and that it fulfills all the requirements of the Code of Conduct and Good Practices of the Universidade de Lisboa.

Acknowledgments

Gostaria de agradecer em primeiro lugar à minha familia por sempre me apoiarem e incentivarem a prosseguir com os meus estudos académicos e por me terem ajudado a chegar onde estou hoje.

Em segundo lugar, gostaria de agradecer tambem ao professor José Carlos Fernandes Pereira, ao Francisco Martins e a toda a equipa do projeto SmokeStorm, pelo contínuo apoio dado ao longo desta tese.

A todos os que conheci na minha estadia no Instituto Superior Técnico, obrigado pela diversão, ajuda que me trouxeram e por tornarem a minha vida cá mais fácil.

Agradeço tambem à Escola Náutica Infante D. Henrique, por me dar a resiliencia e confiança necessária para atacar qualquer problema e situação, mesmo não tendo todas as ferramentas necessárias.

Um enorme obrigado a todos os membros da equipa de Voleibol da AEIST, por fazerem possivel os 3 treinos por semana que me ajudavam a ter força para prosseguir o meu precurso academico, e à ADESL por tornar possivel o campeonato, que me dava uma razão para continuar constantemente a esforçar-me para melhorar.

À malta de Massamá, obrigado pelas montanhas de noites no discord e pelas conversas de meia noite que tornaram possível a minha busca pelo conhecimento e que me faziam o dia.

Por último, quero agradecer à Margarida. Que sem ela, nada disto era possível. Que esteve sempre lá para mim quando as coisas se tornaram difíceis e que nunca desistiu de mim, mesmo quando eu ja o tinha feito. Pelas centenas de desabafos que ouviu e pelo enorme apoio que me deu.

Obrigado.

Resumo

Esta tese tem como objetivo investigar a influência do fluxo de impulsão térmica e da velocidade do vento nas plumas de fumo geradas por incêndios florestais na região próxima à fonte, geralmente dentro de 1 km^3. O efeito da geometria da fonte de fogo também é explorado, embora em menor extensão. Foram realizadas simulações numéricas com uma simulação grandes escalas (LES) utilizando um modelo analógico de libertação de calor para substituir o fogo. O jato quente de baixo momentum interage com a corrente cruzada para diferentes fluxos de impulsão e geometrias da fonte de libertação de calor. Foram comparadas as libertações de calor sensível por transferência de calor em fontes retangulares e em linha.

A análise concentrou-se no comportamento instantâneo da pluma, nos campos de fluxo médios no tempo e na pluma equivalente obtida pela integração da pluma. O fluxo de impulsão da fonte da pluma e a relação entre a velocidade do jato e o escoamento de corrente cruzada influenciam a formação da estrutura vortical coerente presente abaixo da pluma, designada por esteira e vórtices verticais. Um aumento no fluxo de impulsão resulta em maior ascensão e expansão da pluma, bem como numa diminuição dos picos de concentração de fumo a uma determinada distância da fonte.

A pluma efetiva é obtida a partir da integral da concentração de fumo ao longo do vão da pluma, resultando em uma pluma efetiva 2D. Os perfis de concentração integrados concordam satisfatoriamente com o modelo teórico clássico da pluma Gaussiana, e os resultados globais foram considerados satisfatórios.

Para proporções de aspecto elevadas da fonte retangular ou para uma linha de fogo infinita, múltiplos vórtices longitudinais são formados, que se aglutinam até a formação da estrutura de vortice em contra-rotação que caracteriza o campo médio temporal de plumas ou jatos em corrente crusada. O comprimento de onda dos vórtices no sentido do escoamento foi quantificado e mostrou aumentar com o fluxo de impulsão. Os mecanismos de geração do par de vórtices contra-rotativos também foram influenciados pela relação de aspecto da geometria da fonte de calor.

Palavras-chave: Plumas de Fumo, Jatos Flutuantes em Corrente Cruzada, Vórtices de Esteira, Estruturas Vorticais, Vortices Longitudinais, Simulação LES

Abstract

This thesis aims to investigate the influence of the buoyancy flux, crossflow velocity and source geometry smoke plumes generated by wildfires, in the near source region, typically within 1 km^3. Numerical solutions of large eddy simulation LES were performed using an analogue heat release model to replace the fire. The low momentum hot jet in cross flow was predicted for different buoyancy fluxes and geometries of the heat release source. Rectangular and line heat transfer sensible heat releases were compared.

The analysis was focused on the unsteady plume behavior, the time-averaged flow fields and on the equivalent model obtained by integration of the plume. The plume buoyancy flux and jet to crossflow velocity ratio influences the generation of the vertical coherent structures present underneath the plume, designated by wake and upright vortices. An increase of the buoyancy flux results in an increase of plume rise and plume expansion, as well as a decrease in the peaks of smoke concentration at a given distance from the source.

The effective plume is obtained from the integral of the smoke concentration along the plume span resulting in a 2D effective plume. The resulting integrated concentration profiles agree satisfactory with the classical theoretical Gaussian plume model, and the overall results were deemed satisfactory.

For high aspect-ratio of the rectangular source or for an infinite fire line multiple streamwise vortices are formed that coalesce up to the formation of the counter vortex structure that characterizes time averaged fire plumes. The wavelength of the streamwise vortices was quantified and was shown to increase with the buoyancy flux. The generation mechanisms of the counter-rotating vortex pair were also strongly influenced by the heat source aspect ratio.

Keywords: Smoke plumes, Buoyant Jets in Crossflow, Wake Vortices, Vortical Structures, Streak Vortices, LES simulation

Contents

Acknowledgments v

Resumo vii

Contents **xi**

List of Tables **xiii**

List of Figures **xv**

Nomenclature **xix**

1 Introduction **1**

1.1 The Problem and its Relevance. Plume in Crossflow and Vortical structures 1

1.2 Relevant studies, Laboratory experiments, CFD and Field measurements 3

1.3 Objectives 6

1.4 Contributions 6

2 Physical and Numerical Model **7**

2.1 Physical Model 7

2.1.1 Governing equations 7

2.1.2 Large Eddy Simulation 8

2.2 Numerical Model 9

2.2.1 OpenFOAM 9

2.2.1.1 PIMPLE Algorithm 9

2.2.1.2 Finite Volume Method 9

2.2.2 Domain and Boundary Conditions 10

2.2.2.1 Boundary Conditions 10

2.2.2.2 Equivalent Thermal Source 11

3 Validation & Verification **17**

3.1 Atmospheric Boundary Layer 17

3.2 Plane Jet in Crossflow 18

3.3 Meteotron Fire-Plume Experiment 19

3.3.1 Grid Independence study 20

3.3.2 Results 21

4 Results **25**

4.1 Rectangular source plume in a crossflow 25

4.1.1 Unsteady Plume Structure 26

4.1.2 Time-averaged Plume Model 28

4.1.3 Effective Plume Model 34

4.2 Line Fire Plumes 38

4.2.1 Unsteady line plume structure 39

4.2.2 Time-Average Fire Line Plume 42

4.2.3 Effective Plume Model 43

5 Conclusions **49**

5.1 Low aspect-ratio sources 49

5.2 High aspect-ratio sources 49

5.3 Future Work 50

Bibliography **51**

A List of Detailed Boundary Conditions **55**

List of Tables

2.1 Values of the heat-source parameters for the different cases. 14

3.1 Results of the grid independence study performed. 22

4.1 Detailed parameter description of the simulated plumes. 26
4.2 Different simulation cases 26
4.3 The mean maximum vertical velocity of the upright vortices and their frequency for different plume buoyancy fluxes. 28
4.4 Plume expansion angles θ variation with K and Fr 33
4.5 Summary of the inlet parameters for the line fire cases. 39
4.6 Streak vortex wavelength for different cases. 42

List of Figures

1.1 Representation of the different vortical structures of a JICF, taken from Ref [3]. 3

2.1 Typical nested mesh for the plume in crossflow solution. 11

3.1 Comparison of profiles between the present case (solid blue line), Yassin's case (red crosses) and the initial profiles (dashed black line) 18
3.2 Illustrative figure of the flowfield taken from Ref. [30] 19
3.3 Plots of the non-dimensional velocity throughout the height of the channel for different distances from the jet inlet. 19
3.4 Different plume-averaged properties at different heights, as a function of mesh resolution. 21
3.5 Plume-averaged buoyancy flux profiles for different mesh resolutions. 22
3.6 Side-by-side comparison between the present case plume (a)) and the smoke plume calculated by FDS (b), taken from [31]). 22
3.7 Comparison of different plume-averaged properties for plumes with different initial temperatures, with the Meteotron experiment and the FDS simulation 23
3.8 Comparison of the plume-averaged buoyancy flux profile of the different plumes with distinct initial temperatures and the Meteotron experiment. 24

4.1 Visualisation of the vortical structures, via $Q = 0.01$ isosurfaces, for different 4.1(a) Case 7, 4.1(b) Case 8, 4.1(c) Meteotron Case and 4.1(d) shows the vertical velocity close to the ground with white contours of $Q = 0.02$. 27
4.2 $Q = 0.02$ isosurface prediction of the Meteotron Plume color-mapped with the vertical vorticity 4.2(a), streamline representation of the upright vortices 4.2(b) and trajectory of Lagrangian particles released at 10m AGL. 29
4.3 Case 8 $Q = 0.01$ a) isosurface and upstream view with flow streamlines and b) velocity vectors. 30
4.4 Side-by-side comparison between an instantaneous and time-averaged smoke plume, for $K = 1$ and $Fr = 0.52$. 30
4.5 Crossplume smoke concentration profiles. 31
4.6 Profiles of different cross-plume smoke concentrations (kg_{smoke}/kg_{mix}) at different distances from the source (a) 100m, (b) 300m, (c) 500m and (d) 700m 32

4.7 Representations of the expansion and tilt angles for the different plume cases. 32
4.8 Expansion angles 4.8(a) and tilt angles 4.8(b) for the different plume cases. 33
4.9 Plume rise of the different cases. 33
4.10 Plots of maximum plume temperature, vorticity and velocity values at different distances from the source (200m, 400m, 600m and 800m). 34
4.11 Gaussian a) horizontal and b) vertical dispersion coefficient charts. 35
4.12 Effective Plume profiles for each relevant case, at different distances from the source (200m, 400m, 600m and 800m). 36
4.13 Comparison between the effective plume for Case 7 and the equivalent CWI Gaussian plume. 37
4.14 Comparison between the effective plume for Case 8 and the equivalent CWI Gaussian plume. 37
4.15 Comparison between the effective plume for Case 11 and the equivalent CWI Gaussian plume. 38
4.16 Comparison between the effective plume for Case 12 and the equivalent CWI Gaussian plume. 38
4.17 Calculated plume rise (solid grey line) comparison with Briggs's correlation (solid blue line) for cases 5, 6, 7, and 8. 39
4.18 Computational domain of a) the Finite line-fire simulation 3D domain, b) close-up top-view of the heat source, c) computational domain of the infinite line fire case, d) close-u top-view of the infinite heat source. 40
4.19 Instantaneous three-dimensional isosurfaces of a) $Q = 0.2$ and b) $\phi = 10^{-3}$ for case 19. . 40
4.20 a) smoke concentration contours for Case 16 at $x = 150m$, where b) shows a zoomed up image of the concentration with line contours of the smoke concentration. 41
4.21 Comparison between the streak vortex wavelengths, as a function of wavelength, obtained by Finney in [17] and the ones calculated in cases 16, 18 and 19, depicted by purple triangle, square and dot, respectively. 43
4.22 Time-average line fire and rectangular plume smoke contour comparison with $K = 2$ and $Fr = 0.478$. 44
4.23 Time-average streamwise vorticity contours for different distances from the source and 400m span for: case 17 a), b) and c); case 18 d), e) and f); case 19 g), h) and i). 44
4.24 Streamwise vorticity slices at $x = 900m$ with $700m$ span and smoke concentration contours. 45
4.25 Effective plume smoke concentration (kg/kg) profile for the infinite line fire (Case 16). . . 45
4.26 Effective plume smoke concentration (kg_{smoke}/kg_{mix}) for Case 17 (4.26(a)), Case 18 (4.26(b)) and Case 19 (4.26(c)) at $x = 200m$, $x = 400m$, $x = 600m$ and $x = 800m$. 46
4.27 Effective plume concentration comparison with the gaussian model plume for 4.27(a) case 17, 4.27(b) case 18 and 4.27(c) case 19 at $200m$, $400m$, $600m$ and $800m$ from the source. 47

A.1 Velocity boundary conditions. 56

A.2 Temperature boundary conditions. 57
A.3 Passive smoke scalar boundary conditions. 58
A.4 Total pressure boundary conditions. 59
A.5 p_{rgh} boundary conditions. 60
A.6 p_{hrgh} boundary conditions. 61
A.7 Turbulent kinetic energy boundary conditions. 62
A.8 Turbulent kinematic viscosity boundary conditions. 63
A.9 Turbulent thermal diffusivity α_T Boundary Conditions. 64
A.10 N_2 specie boundary conditions. 65
A.11 O_2 specie boundary conditions. 66

Nomenclature

Acronyms

ABL	Atmospheric Boundary Layer
AGL	Above Ground Level
BJCF	Buoyant Jet in a CrossFlow
CFD	Computational Fluid Dynamics
CRVP	Counter-Rotating Vortex Pair
CWI	Cross-Wind Integration
FDS	Fire Dynamics Simulator
FVM	Finite Volume Method
GCI	Grid Convergence Index
HRR	Heat Release Rate
HSV	Horse-Shoe Vortex
JICF	Jet In a CrossFlow
LES	Large Eddy Simulation
OpenFOAM	Open Field Operation And Manipulation
PISO	Pressure Implicit with Split Operator
RANS	Reynolds Averaged Navier-Stokes
SIMPLE	Semi-Implicit Method for Pressure Linked Equations
SLV	Shear Layer Vortex
TVD	Total Variation Diminishing
URANS	Unsteady Reynolds Averaged Navier-Stokes
WV	Wake Vortex

Greek symbols

α Thermal expansion coefficient $[K^{-1}]$

β Tilt angle $[^\circ]$

ϵ Relative error

Γ General diffusive term

κ Von Kármán constant

μ Dynamic viscosity $[kg/ms]$

ν Kinematic viscosity $[m^2/s]$

ϕ General variable

ρ Density $[kg/m^3]$

τ Viscous stress tensor $[N/m^2]$

θ Expansion angle $[^\circ]$

Operators

Δ Change in variable

$\nabla \cdot \vec{U}$ Divergence

$\nabla\phi$ Gradient

∂ Partial derivative

$\propto$ Proportionality

Roman symbols

C Gaussian model smoke concentration $[kg_{smoke}/kg_{mixture}]$

C_e Sub grid scale model coefficient

C_k Sub grid scale model coefficient

C_{mu} Constant

D Diameter $[m]$

F_B Buoyancy flux $[m^4/s^3]$

F_s Safety factor

Fr Froude number

g Gravitational acceleration $[m/s^2]$

Gr	Grashof number
h	Enthalpy $[J/kg]$
I	Turbulence intensity
I_B	Byram's Intensity $[W/m]$
J	Momentum flux ratio
K	Velocity ratio
k	Turbulent kinetic energy $[m^2/s^2]$
L_t	Heat source thickness $[m]$
p	Pressure $[Pa]$
p_{hrgh}	Non linear component of the hydrostatic pressure $[Pa]$
p_{rgh}	Static pressure $[Pa]$
Q	Q-criterion
R	Gas constant $[J/kgK]$
Re	Reynolds number
Ri	Richardson number
S	Source term
T	Temperature $[K]$
t	Time $[s]$
u^*	Friction velocity $[m/s]$
u_r	Relative velocity $[m/s]$
y_0	Aerodynamic roughness $[m]$
z_j	Jet rise $[m]$
z_{plume}	Plume rise $[m]$
$\vec{U}$	Velocity vector $[m/s]$
u, v, w	Velocity Cartesian components $[m/s]$

Subscripts

0	Initial plume condition
∞	Free-stream condition

exp Experimental values

f Face of the control volume

i, j, k Computational indexes

n Normal component

x, y, z Cartesian components

Chapter 1

Introduction

1.1 The Problem and its Relevance. Plume in Crossflow and Vortical structures

Wildfires are a major concern for countries with dry weather, strong winds and especially during the summer time when peak temperatures keep breaking records every year. Portugal is a perfect example of the latter two, with huge wildfires occurring every year during the months of higher temperatures. Just a few years back, there was the Pedrógão Grande wildfire that caused several fatalities and destroyed homes, dislocating thousands of people. An overall burned area of 53 000 ha gave it the title of ”Portugal’s largest wildfire”. Specialists say that the deaths of some of these people were caused by smoke inhalation, rather than getting caught in the fire itself. This makes it important to study the smoke trajectory and dispersion, to know how the smoke propagates through the nearby land to alert people in the surrounding areas and to safely evacuate them.

Vegetation fires release hot gases and particles that rise due to the heat from combustion. The final height of the smoke plumes is determined by the atmosphere’s thermodynamic stability and the fire’s heat output. In mesoscale simulations of fire plumes, where the path of the smoke is calculated over several hundreds of kilometers, the details of the near region of the plume origin can not be resolved due to the mesh sizes used, of several hundreds meters, or even kilometers. In predictions, the priority is to understand if the plume rises up to stratosphere to be casted into the global circulation and travel thousands of kilometers.

Consequently correlations or 1-D models have been developed that calculate the plume height and the diameter to allow to estimate the smoke concentration profile. The 1-D plume model is integrated into each column of 3-D low-resolution atmospheric chemistry-transport models to determine the smoke injection height, allowing trace gases and aerosols from vegetation fires to be released, transported, and dispersed by the simulated prevailing winds. One of the most successful 1-D models was developed by Freitas et al. [1] [2], that simulates the vertical transport of hot gases and particles from vegetation fires, accounting for the impact of environmental wind on smoke plume transport and dilution. The model calculates the plume radius, the plume rise over time, and the smoke injection height. These classes of integral models can not be used for the fire smoke plume in the near field of the source of the fire because it neglects the complexity of the unsteadiness and interaction of the formed vortical structures from the interaction of the buoyancy and the crosswind.

Fire plumes are driven by buoyancy at the fire source and, by interacting with the atmospheric boundary layer curve and asymptotically reach their equilibrium height, depending on the atmospheric stability. Depending on the buoyancy flux and crossflow, the plume's curvature during the rising motion is determined. Strong horizontal winds can increase lateral spread and drag, especially for smaller fires, affecting the smoke's vertical rise. The near field of the fire plume, say in a volume of 1 km^3, is of great relevance to understand the role of the multiple vortical structures on the plume rise and the smoke dispersion. The understanding of these structures is crucial for firemen and decision-makers to take action in the urban interface. The problem to be considered in this work is a thermal plume in crossflow, because the main influencing factors of smoke plume dispersion that were just described are present. The literature shows that the effect of crossflow has been continuously investigated, particularly for isothermal Jets In CrossFlow (JICF), but the role of the heat release on the 3-D plume formation is much less studied. Despite that, it is well known that the main vortical structures that govern the instantaneous flow field of JICF are also present in plumes in crossflow. There are 4 dominant vortex systems, depicted in Figure 1.1:

1. Horse Shoe Vortex (HSV): This is a vortex generated near jet inlet that wraps around the jet. This vortex is caused by the roll up of the boundary layer and is very hard to capture with a coarser mesh, since it is necessary to solve the boundary layer to obtain the HSV;

2. Shear Layer Vortices (SLV): The SLV are formed by the shear instability between the jet and the crossflow right as the jet enters the freestream, similarly to a Kelvin-Helmholtz instability. There are transient vortices that move throughout the structure so they can only be captured in the instantaneous field and not in the time averaged ones.

3. Wake Vortices (WV): These vortices have been a subject of many studies in the past and there is still no clear consensus on how they are generated. They seem to be vortices shed by the jet and are also convected downstream by the crossflow. However Fric and Roshko [3] have documented that these vortices are not actually shed by the jet itself, but by the boundary layer instead. If the jet entrainment is strong enough these vortices can be stretched towards the jet structure, entraining fluid into the jet. If this happens the vortices are called Upright Vortices (UV). However,in older documentation this nomenclature does not exist and the terms "upright" and "wake" vortices are used analogously.

4. Counter-Rotating Vortex Pair (CRVP): The CRVP is a vortex system comprised of two vortices side by side with oposite orientation and the same magnitude. There has also been no definitive conclusion on how this vortex system is generated. The most widely accepted explanation was given by Kelso et al. [4], who has suggested that the CRVP is formed by the roll-up of the shear layer vortices caused by the interaction between the vortex rings and the crossflow. This vortex

system is the largest and most dominant vortex system in the flow, and it is also a steady structure, making it possible to be captured and observed in the time averaged fields.

All of these vortex systems interact with each other and this interaction affects the flow and trajectory of the plume, which is what makes their dynamics so complex.

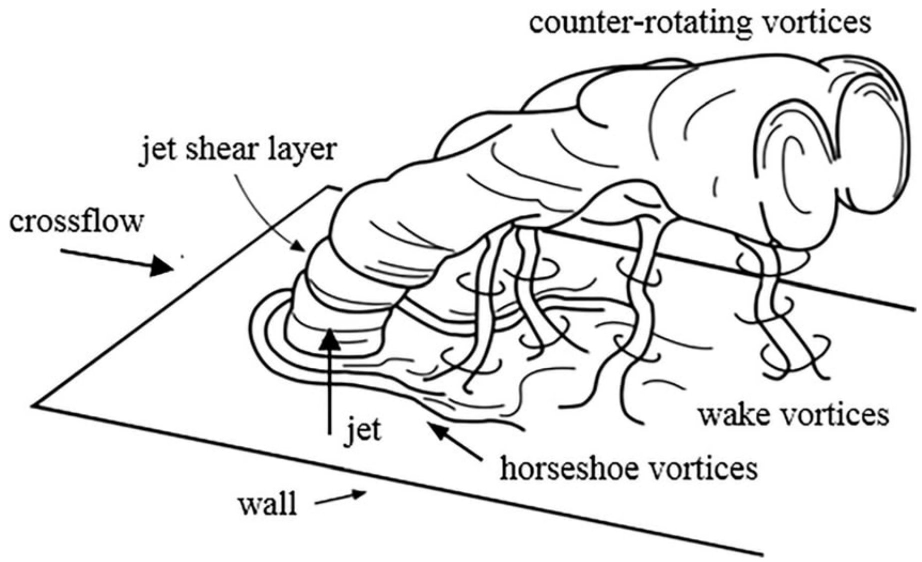

Figure 1.1: Representation of the different vortical structures of a JICF, taken from Ref [3].

1.2 Relevant studies, Laboratory experiments, CFD and Field measurements

Throughout the years, many studies and observations have been conducted around the topic of wildfires and plume propagation and it's necessary to review this literature to get a better grasp on the subject and to be able to understand the complex world of wildfire smoke propagation. In 1965 G.A. Briggs [5] performed a dimensional analysis to predict the plume rise of buoyant plumes, more directed at chemical chimney smoke. He concluded that the dominant terms for the plume rise are the buoyant flux, the wind speed and the stability of the atmosphere. He developed plume rise expressions for both stable and neutral conditions and for the plume trajectory while it is still transitioning to a fully developed plume. Most of his expressions are supported by observations mentioned in his work except for the final plume rise in a neutral atmosphere. Later on, another paper was published where the previous expressions were adjusted to obtain better predictions.

Fric and Roshko [3] published a paper on the vortical structures in JICF, with the main focus being the study of wake vortex formation and their differences from vortex generation downstream of a cylinder flow. From the experiments conducted, it was demonstrated that, although the wake vortices from the leeward side of the jet may look similar to the ones created in the wake of a cylinder, their formation mechanisms are not the same. While the vortices in a cylinder wake are generated from the shedding the boundary layer around the cylinder, the JICF wake vortices come from the shedding of the ground boundary layer. Moussa et al. [6] supported this statement and measured the frequency of wake vortex generation from a skirted and a non-skirted jet inlet in various experiments and found that the non-skirted pipe had a constant Strouhal of 0.2, very similarly to the case of a regular cylinder. However, the skirted inlet showed that the Strouhal number varies with the velocity ratio between jet and crossflow, K. This supports the Roshko's wake vortex generation hypothesis. Kelso [4] also performed an experimental study on round jets in crossflow using flow visualization techniques and flying-hot-wire measurements in laminar flows, in order to better understand the formation and interaction of these different vortex systems. Kelso reports that the vortex rings, formed in the shear layer between the jet and the cross-stream, collapse and break-down when interacting with the crossflow, and this creates the CRVP and the Wake Vortices. It's also shown that the vortex street formed on the wake of the plume is not always organized and can have different configurations depending on the flow Reynolds number and on the velocity ratio between the plume and the crossflow. This is also something that Roshko mentions in his work.

The phenomenon of plume bifurcation, has been reported in several naturally occurring plumes but is not yet fully understood. In 1994 Gerald Ernst, John P. Davis and R. Stephen Sparks published a study on the bifurcation of vulcanic plumes in cross-winds [7] and they suggest that the separation the counter-rotating vortices is induced by the low pressure in the sides of the plume, caused by the high speeds of the crossflow. They also suggest that some of the parameters that can affect bifurcation are: the effects of buoyancy (this has been supported by Scorer [8] and Turner [9]); the release of latent heat from the evaporation of water droplets present in vulcanic plumes which cools the outside of the CRVP increasing circulation; collision of the plume with high density boundaries; source geometry and orientation of the plume. Taizo Hayashi [10] experimentally reported the bifurcation of bent over plumes by injecting colored alcohol into a flume with circulating water and studied the effect of various parameters and recorded whether the plume had been bifurcated or not each occurring in very distinct conditions of the plume's Froude number and plume to crossflow velocity ratio. The Froude number is a parameter that determines if the flow is buoyancy ($Fr < 1$) or momentum driven ($Fr > 1$). For higher Froude numbers and lower velocity ratios, no bifurcation occurs. For higher velocity ratios and lower Froudes an eliptical profile is created. And in between there is a small region of well distinct plume bifurcation. Yafei Lv et al. [11] investigated the interactions of the vortex structures generated in a JICF and the effect of the velocity ratio. They were able to establish a maximum and a minimum value for the velocity ratio for the CRVP to be able to form. If the jet velocity is too weak, the jet will bend over quickly close to the jet exit and will spread over the wall. However if the jet velocity is too high, the CRVP gets broken down into finer scale vortices due to the strong shear it is subjected to, causing instability in the interface between the jet and the crossflow and formation of shear layer vortices.

Pablo Huq and M. R. Dhanak [12] performed an experimental study of a laminar circular JICF and have reported that jet bifurcation occurs when $K \geq 4$. They mentioned that for jets where the velocity ratio is lower than 4 the jet does not bifurcate and the flow is instead governed by tangled vortical structures. This was thought to be caused by the wake of the cylinder protruding into the crossflow, through which the jet is injected into the domain. They were also able to predict the bifurcation point through potential flow models and bifurcating elliptical jets and concluded that for higher velocity ratios, bifurcation occurs further from the jet inlet. By analyzing the time-averaged scalar concentration contours at a certain distance from the inlet, the results suggested that the dilution is larger for bifurcated jets than for non-bifurcating jets. Howard R. Baum [13] numerically simulated a plume with Lagrangian particle injection to simulate the smoke's particulate matter emission. He concluded that, for a stably stratified atmosphere, the smoke will be further dispersed due to the Brunt-Väisällä frequency. This, together with the diminishing strength of the CRVP, will destroy the plume bifurcation and generate a somewhat uniform smoke profile. However this occurs far downstream of the source. Baum also published another study [14] regarding multiple plume interactions and showed that these interactions are non-linear and often cause particulate matter to be propagated to unexpected places, affecting the plume rise and smoke concentration profile. This makes it so that some plume models become less accurate or even unreliable in predicting the plume propagation. But like in his previous paper, he showed that far downstream, when the CRVP vorticity decreases, the smoke profile becomes somewhat uniform. The downstream distance from the fire source at which this occurs will depend on the number of plumes and their position.

Haines and Smith [15] have made field observations of three coherent vortical structures formed by intense wildland fires. In their work there are images of these different vortical structures, that were formed during wildfires, including images of bifurcated plumes and they attempt to explain the formation of these structures. Church and Snow [16] have also studied the formation of vortical structures, but this time in a controlled environment using the Meteotron apparatus. Fuel oil burners were used in order to generate a 1000 MW thermal plume. Three vortical structures were observed: the counter rotating vortex pair, strong small scale vortices resembling dust devils, and large columnar vortices. They discuss the mechanisms of vortex generation, such as stretching and tilting of horizontal vorticity present in the wind and the generation of vorticity due to buoyancy.

Finney et al. [17] focused on a saw-toothed flame structure, followed by streaks of smoke behind it, that had been repeatedly seen in laboratory and field-scale fires. Employing high-speed imaging they were able to identify that these structures were a product of several CRVP's interacting with each-other causing the flames to be down-washed in certain regions and lifting up in others. This up and down-washing of flames was given the name of ”towers and throughs” but may also be called ”crests and throughs” or ”peaks and valleys” in different literature. In addition, Finney conducted an experiment using a heat source simulate a linefire and the obtained results show that, not only a non-reactive laboratory-scale flow can be scaled into a large-scale fire according to their scaling method, but the main vortical structures are present in non-reactive flows as well. D. Morvan [18] performed a numerical study of a laboratory-scale, homogeneous line fire with intention of seeing if these laboratory scale fires could be scaled to field scale cases. He found that there is a very good scalability, based on the fire's Byram and Froude numbers. He also found that the origin of the crests and throughs' structure comes from the attempt of the flow to balance the buoyant forces of the thermal plumes and the inertial forces of the wind.

1.3 Objectives

Since the topic of buoyant plumes in crossflow is still not fully understood, the main objective in this thesis is to expand on this topic and to better understand the formation of vortical structures in plumes from forest fires, in the fire's near region of 1 km^3, and how these can vary with the plume's buoyancy flux and the source's geometry. This includes a low and high aspect-ratio rectangular source and a continuous line of heat release. Emphasis is given to the effect of the previously mentioned uncertainties in the smoke transport and dispersion in the near region, comparing the effective plume with the ones provided by Gaussian models.

The simulations investigate the effect of the buoyancy flux on the plume dynamics in a medium scale distance from the fire, typically up to 1km from the fire.

1.4 Contributions

Numerical simulations of different large scale plume in crossflow scenarios were performed. These scenarios include a plume issuing from a rectangular source, with a relatively small aspect-ratio, an infinite line source and a high aspect-ratio rectangular source.

The analysis of the unsteady vortices and the time-averaged flow (temperature, smoke concentration, velocity, plume rise, expansion and tilting) is made. The effective plume characteristics are also obtained, using an integral approach of the plume, and mainly allows to verify the Gaussian plume distribution assumption to provide smoke concentration profiles at the plume's asymptotic height. The effect of the fire source geometry, in particular high aspect-ratio sources and an infinite line fire, is quantified at instantaneous and time-averaged flow fields and also at equivalent plume configurations considered in integral plume models.

Chapter 2

Physical and Numerical Model

2.1 Physical Model

In this section, a description of the governing equations, domain geometry, boundary conditions, scaling parameters and assumptions used will be performed.

2.1.1 Governing equations

The flows presented in this thesis are described by the set of Continuity 2.1, Momentum (Navier-Stokes) 2.2 and Energy 2.3 conservation equations, written as:

$$\frac{\partial \rho}{\partial t} + \rho \left(\nabla \cdot \vec{U} \right) = 0 \tag{2.1}$$

$$\frac{\partial \rho \vec{U}}{\partial t} + (\rho \vec{U} \cdot \nabla)\vec{U} = \rho \vec{g} - \nabla p + \mu \nabla^2 \vec{U}, \tag{2.2}$$

$$\frac{\partial \rho h}{\partial t} + \nabla \cdot (\rho h \vec{U}) = -\frac{\partial p}{\partial t} + \nabla \cdot (k \nabla T) + \phi \tag{2.3}$$

where ρ is the density of the fluid, t is time, $\vec{U}$ is the velocity vector (u, v, w), $\vec{g}$ is the gravitational acceleration vector, p is the pressure, μ is the dynamic viscosity of the fluid, h is the total enthalpy, k is the thermal conductivity, T is the temperature and ϕ is a source term. As mentioned in Section 2.2.2, radiation was neglected. Thus no radiation term was considered in the energy conservation equation.

A scalar transport equation is used to model smoke dispersion

$$\frac{\partial \rho \phi}{\partial t} = \nabla \cdot \left(\rho \vec{U} \phi \right) - \nabla \cdot \Gamma \nabla \phi \tag{2.4}$$

where ϕ is the smoke concentration and J is the scalar diffusivity. By using this equation, the smoke is being considered a passive scalar.

2.1.2 Large Eddy Simulation

The flows predicted in this work are highly turbulent and unsteady, so an approach to model the turbulence is required. Large Eddy Simulation (LES) was chosen because this method allows for higher precision when compared to Unsteady Reynolds Averaged Navier-Stokes (URANS) calculations, but increases the computational cost of the 3-D calculation greatly. Large Eddy Simulations are able to distinguish small eddies, which are nearly isotropic, and large eddies, which can be highly anisotropic and interact and extract energy with the mean flow. While in Reynolds Averaged Navier-Stokes (RANS), all eddies are solved by the same turbulence model, in LES large eddies are computed in a time dependent approach. On the other hand, the influence of the small eddies on the flow can be captured by using a compact model.

To distinguish between large eddies and small eddies, LES uses a spatial filter defined by the grid size. This is the reason why this method is more costly than the former. The grid defines the cutoff width Δ, at which eddies larger than it will be resolved with unsteady flow computation, while the smaller ones will not be computed.

The filtered continuity and momentum equations are given by 2.5 and 2.6, respectively.

$$\frac{\partial}{\partial x_i}(\rho\overline{u_i}) = 0 \tag{2.5}$$

$$\frac{\partial}{\partial t}(\rho\overline{u_i}) + \frac{\partial}{\partial}(\rho\overline{u_i u_j}) = -\frac{\partial\overline{p}}{\partial x_i} + \frac{\partial}{\partial x_j}\left[\mu\left(\frac{\partial\overline{u}_i}{\partial x_i} + \frac{\partial\overline{u}_j}{\partial x_i} - \frac{2}{3}\delta_{ij}\frac{\partial\overline{u}_l}{\partial x_l}\right)\right] - \frac{\partial\tau_{ij}}{\partial x_j} \tag{2.6}$$

where τ_{ij} is the Sub-Grid-Scale stresses, which result from the filtering process and are unknown.

To make up for the influence of the small eddies and to obtain τ_{ij} a Sub-Grid-Scale (SGS) model is employed.

$$\tau_{ij} = -2\mu_{SGS}\overline{S}_{ij} + \frac{1}{3}\tau_{ii}\delta_{ij} = -\mu_{SGS}\left(\frac{\partial\overline{u}_i}{x_j} + \frac{\partial\overline{u}_j}{x_i}\right) + \frac{1}{3}\tau_{ii}\delta_{ij} \tag{2.7}$$

$$\mu_{SGS} = \rho C'_{SGS}\Delta\sqrt{k_{SGS}} \tag{2.8}$$

where μ_{SGS} is the SGS viscosity, $\overline{S}_{ij}$ is the rate-of-strain tensor and C'_{SGS} is a constant.

The SGS model used is a one equation model developed by Akira Yoshizawa [19]. It includes a turbulent kinetic energy transport equation to take into account the effects of convection, diffusion, production and destruction on the sub-grid scale, given by Equation 2.9 which allows for the calculation of the SGS stresses by using the following expressions.

$$\frac{\partial}{\partial t}\rho k_{SGS} = \nabla\cdot(\rho D_k\nabla k_{SGS}) + \rho G - \frac{2}{3}\rho k_{SGS}\nabla\cdot u - \frac{C_e\rho k^{1.5}}{\Delta} \tag{2.9}$$

where k_{SGS} is the SGS turbulent kinetic energy, D_k is the turbulent diffusivity, C_e and C_k are model coefficients with a value of 1.024 and 0.094 respectively.

2.2 Numerical Model

In this section, a description of the numerical models and methods used to solve the 3D simulations is made, as well as a documentation of the numerical boundary conditions used.

2.2.1 OpenFOAM

In this work, the tool used to solve the governing equations was OpenFOAM [20] (versions 4.1 and 8). This is an open-source CFD software which allows the user to solve several types of flows by offering multiple solvers to be used. In this case, the solver used to perform the calculations was FireFOAM, which is a transient solver widely used to simulate fire and turbulent buoyant plume dynamics. This solver makes use of the Favre filtered Navier-Stokes equations, which is convenient, given that the turbulent fluid flows simulated in this thesis feature large temperature and density gradients.

2.2.1.1 PIMPLE Algorithm

The iterative procedure of solving the Navier-Stokes equations was performed using the PIMPLE algorithm. This algorithm was created by merging the transient PISO [21] (Pressure Implicit with Splitting-Operator) and the steady-state SIMPLE [22] (Semi-Implicit Method for Pressure-Linked Equations). Within every timestep, the equations are iteratively solved into a more converged solution, and when the desired convergence level is achieved, it moves on to the next time-step. To do this, in every outer iteration, the momentum and energy equations are solved once and the pressure correction equation may be solved several times (in an inner loop), performing the explicit PISO correction to the pressure and velocity fields. This process continues until both pressure and momentum are converged and the next time-step can be calculated.

2.2.1.2 Finite Volume Method

To discretize the governing equations, OpenFOAM uses the Finite Volume Method (FVM). This method allows for the discretization of the computational domain into multiple different control volumes. The conservation equations, for example the generic scalar transport equation, are integrated over those control volumes. When possible, the divergence and Stokes theorems are applied, which yields

$$\frac{\partial}{\partial t}\int_V \rho\phi\partial V + \int_A \rho u\phi\partial A = \int_A \Gamma\nabla\phi\partial A + \int_V S_\phi\partial V \tag{2.10}$$

where V is the the volume of the control volume, A is the surface area on the face of the control volume, ϕ is a generic scalar quantity to be replaced with the different physical quantities to be conserved and u is the velocity component normal to the face of the control volume.

These equations are then discretized in the control volume where the values on the faces of each control volume are obtained from the ones on the centroid, using a numerical scheme. This turns the set of partial differential equations to be solved, into a set of algebraic systems of equations which can be solved numerically.

2.2.2 Domain and Boundary Conditions

The cases simulated are wildfire analogues, in an open field with constant and uniform wind. The domain of interest is reasonably large, with focus on the plume dynamics up to 1 kilometer downwind from the source. In order to accurately capture the flow physics in domains of this size, special care must be taken when setting up the boundary conditions, due to large hydrostatic pressure induced density gradients.

Several key simplifications were considered throughout this work in order to better suit the computational resources available. The first simplification was to substitute the wildfire for a hot buoyant jet injection from the ground into the domain of interest. This is an accurate representation of a wildfire for the size of the domain considered, since the focus of this work is the smoke plume and not the fire-front dynamics which would require pyrolisis and combustion of the evaporated gases to be modeled. Very often the plume characteristics are given by a heat transfer analogy (see section 2.2.2.2). Since no flame is being calculated, radiation was also neglected.

2.2.2.1 Boundary Conditions

To setup the simulation, a set of numeric boundary conditions are required. FireFOAM provides a large number of boundary condition (BC) options to pick from. Unlike other commercial CFD software, OpenFOAM requires the boundary conditions to be manually set for every domain boundary and quantity. Because of this, it is important to pick and test various sets of boundary conditions before running the calculations, to make sure that they are correctly set up to reflect the problem that is expected to simulated and that they are compatible with each other and don't cause convergence or numerical problems.

A quick summary of the boundary conditions used is shown below. For the fully detailed boundary conditions, refer to Appendix A.

- Crossflow and plume inlets: Fixed velocity and temperature;
- Ground: No-slip velocity and adiabatic;
- Lateral boundaries: Pressure or cyclic boundary conditions, depending on the study case, as will be referenced in the Results section;
- Top boundary: pressure boundary condition.

In the boundaries where the pressure was specified, the static pressure was computed by subtracting the hydrostatic pressure and the dynamic pressure from the total pressure (in OpenFOAM this is the *prghTotalHydrostaticPressure* BC). Correctly setting the conditions for these boundaries was, by far, the most challenging part of the setup due to the lack of documentation on the different OpenFOAM boundary conditions.

FireFOAM splits the pressure into 3 components, and these components need to be well understood, as well as their boundary conditions.

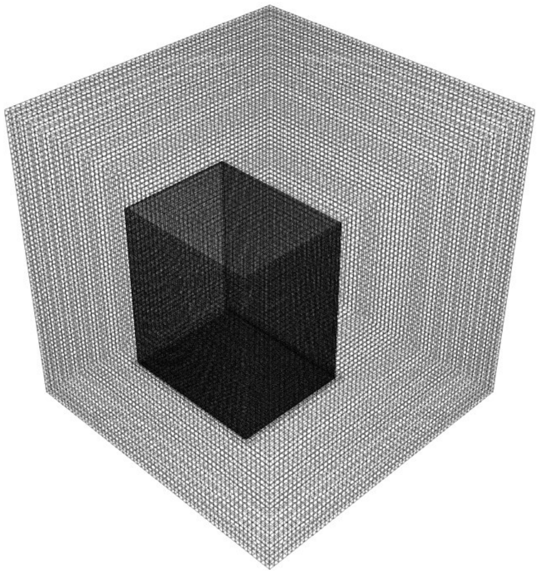

Figure 2.1: Typical nested mesh for the plume in crossflow solution.

- p, the total pressure field.

- p_{hrgh}, the non-linear component of the hydrostatic pressure field which is iteratively initialized at the beginning of the simulation and is used only to assign values to the p_{rgh} open boundary conditions which will be discussed later. It is given by $p_{hrgh} = \rho_0 gh - p_{hydrostatic}$, where ρ_0 is the fluid density at a reference height and pressure. Therefore, p_{hrgh} gives the negative of the pressure gradient due to the fluid's specific mass variation from the pressure.

- p_{rgh}, the static pressure field minus the linear component of the variation of the hydrostatic pressure, computed from $p_{static} = p - \rho_0 gh - 0.5\rho u^2$.

This was not mentioned in the FireFOAM guide manual and was figured out during the lengthy trial and error process of setting up the different BC's. In smaller domain, the flow is not as sensitive to the choice of pressure BC, since the non-linear component of the hydrostatic variation is negligible. However, due to the large dimension of the domains used in this study, the incorrect hydrostatic initializaton would result in non-physical flow predictions.

Different numerical grids were used and a verification and validation study is presented in the next chapter. Figure 2.1 shows an example of the nested mesh used, where a larger concentration of points is located in the vicinity of the plume source, to better resolve the flow structure in this area. Typically, a 1.5 million cell mesh is appropriated to resolve these types of flows, using this type of mesh (as shown in the next chapter).

2.2.2.2 Equivalent Thermal Source

Fire Intensity

The fire intensity of a virtual forest fire can be estimated by Byram's intensity formula:

$$I_B = m\Delta HROS \tag{2.11}$$

where m is the fuel load. Typically, $m = 7kg/m^3$, the rate of spread $ROS = 8.5m/min$ and ΔH is the heat yield of the fuel and is estimated to be $18000kJ/kg$. With this, the Byram's fireline intensity is equal to $I_B = 17.85MW/m$. This value will be considered as the fire intensity to study in the present work of smoke plumes. The value of $I_B = 17.85MW/m$ was selected to represent an eruptive fire.

The focus of the present study is to predict the interaction between the crosswind and the buoyant plumes. The combustion of the fire was replaced by an equivalent fire intensity, given by the above Byram's formula 2.11.

There are many different analogy models such as: low-momentum heat jets, heat released by an energy equation source at the ground or in a pyramid with constant heat-release layers. Here, the first option was applied using a rectangular inlet of different sizes, depending on the study case. Three sources were considered, with areas of 20x$10m^2$, 200x$10m^2$ and an infinite line with $10m$ thickness. The heat release power is given by

$$P = I_B L \tag{2.12}$$

with I_B as the Byram's intensity and L being the fire line length. With the low-momentum jet, the power supplied to the 3D computational domain is $P = \rho_0 u_0 A c_p T_0$. Using the Ideal Gas assumption $p = \rho RT$, and for constant pressure, $\rho T = constant$. This means that $\rho_0 T_0 = constant$ and the initial plume temperature can be changed without varying the power P.

For $u_0 = 5m/s$, $c_p = 1.005kJ/kgK$, $T_0 = 1000K$, $\rho_0 = 0.353kg/m^3$ and an inlet area of $200m^2$, the obtained plume power yields $P = 355MW$. This high value was deliberately chosen to investigate the behavior of fire plumes resulting from massive fires.

Eruptive fires overwhelm the capacity of control, with fireline intensities $> 10MW/m$, rates of spread of $> 50m/min$ and erratic and unpredictable fire behavior and spread. The Pedrógão Grande 2017 was a catastrophic fire, see [23], with 65 fatalities, more than 200 injured people, 458 structures destroyed, burned $45328ha$ of land and had intensities from 20 to $60MW/m$, with a rate of spread of $65m/min$ (see [24]).

Scaling Parameters and Volume Fluxes Modeling

The use of scaling parameters is crucial to represent plume behavior when certain inlet parameters or enviornment conditions are changed. The relevant non-dimensional numbers are the Froude number 2.13, given by Fan [25], the velocity ratio, K and the Reynold's number, Re. These are presented in 2.17 and 2.14, respectively.

$$Fr = \frac{u_0}{\sqrt{\frac{\rho_\infty - \rho_0}{\rho_\infty} gD}} \tag{2.13}$$

where u_0 is the initial jet velocity, ρ_∞ and ρ_0 the densities of the crossflow and jet respectfully, and D is the hydraulic diameter of the jet inlet.

$$Re = \frac{u_\infty L}{\nu} \tag{2.14}$$

u_∞ is the freestream velocity of the fluid, L the length scale of the fluid inlet and ν the kinematic viscosity of the fluid.

Other non-dimensional numbers that may be used in other literature are the momentum flux ratio, usually treated by J (shown in 2.15), that measures the strength of the jet relative to the crossflow, the jet to crossflow velocity ratio, K and the Grashof number 2.16, Gr which represents the ratio of buoyant to viscous forces acting on the fluid.

$$J = \frac{\rho_0 u_0^2}{\rho_\infty u_\infty^2} \tag{2.15}$$

$$Gr = \frac{g\beta(T_0 - T_\infty)L^3}{\nu^2} \tag{2.16}$$

$$K = \frac{u_0}{u_\infty} \tag{2.17}$$

where β is the volume expansion coefficient of the plume and L is the specific length. The velocity ratio K can also be described as $\rho_0 u_0/\rho_\infty u_\infty$. This is usually used in cases where the jet and the crossflow have different densities.

In order to account for strong density and temperature differences, the momentum flux ratio J is often denoted in the form of

$$R = \sqrt{\frac{\rho_0 u_0^2}{\rho_\infty u_\infty^2}} \tag{2.18}$$

and R is used to identify the different flow regimes. For $R < 2$, the momentum is very small and the jet does not penetrate deeply into the crossflow.

The Richardson number, Ri (seen in 2.19) provides information about the ratio of free to forced convection and if $Ri << 1$ then buoyancy effects can be neglected.

$$Ri = \frac{Gr}{Re^2} \tag{2.19}$$

The parametric characterization of the buoyancy dominated regime is most relevant to the study of fire plumes. There are different analyses to perform this parametric identification. Large values of the Byram's convective number, given by

$$N_C = \frac{2gI_B}{\rho_0 c_p T_0 (u_\infty - ROS)^3} \tag{2.20}$$

indicate that fires are governed by plumes. Small values of N_C identify the fire as being wind driven with a dominant role of convection heat transfer. For the present case, in comparison with the cross wind speed, the ROS can be neglected and even so $N_C \approx 100$. Corresponding to a buoyancy dominated regime or plume regime.

Morton characterizes buoyant plumes in terms of a source parameter Γ, which is the inverse square of the Froude number, and can be written as

$$\Gamma = \frac{5Q_0B_0}{8\sqrt{\pi}\alpha M_0^{5/2}} = \frac{1}{Fr^2} \tag{2.21}$$

where B_0, M_0 and Q_0 denote the intitial fluxes of buoyancy, momentum and volume, respectively and α is an entrainment constant with a typical value of $\alpha = 0.1$ (see [26]).

Forced plumes correspond to $0 < \Gamma < 1$, pure plumes $\Gamma = 1$ and for lazy plumes $Gamma > 1$. Taking the values at the source of the present standard case:

$$Q_0 = u_0 A = 1000 m^3/s \tag{2.22}$$

$$B_0 = Q_0 g \frac{\rho_\infty - \rho_0}{\rho_\infty} = 9800 m^4/s^3 \tag{2.23}$$

$$Q_0 = A u_0^2 = 5000 m^4/s^2 \tag{2.24}$$

which gives $\Gamma = 17.5$, confirming the lazy plume under study, see [26] and [27]).

In the presented study the focus is to study the buoyancy flux (Equation 2.25) influence on the plume, and so the inlet temperature is changed whilst maintaining the same velocity.

$$F_B = uAg\frac{T_0 - T_\infty}{T_\infty} \tag{2.25}$$

The different heat sources addressed in this study, characterized by different buoyancy fluxes are listed in Table 2.1.

Table 2.1: Values of the heat-source parameters for the different cases.

T_0 (K)	ρ_0 (kg/m^3)	$\rho_\infty - \rho_0$ (kg/m^3)	Fr	Ri	H (MW/m^2)	F_B (m^4/s^3)
350	1.00	0.176	1.27	0.44	0.252	1 632
500	0.706	0.47	0.47	1.68	0.713	6 393
1000	0.353	0.813	0.50	5.96	1.247	32 386
1900	0.185	0.991	0.22	13.53	1.494	51 997

The plume rise centerline and crosswind observed in real forest fires is very often used to estimate the source buoyancy flux, as detailed in [28]. From the definition of buoyancy flux 2.25, one may write that the sensible heat flux can be given by

$$H = \left(\frac{\rho_\infty c_p T_\infty}{Ag}\right) F_0 \tag{2.26}$$

And so, this yields

$$H = \rho_0 u_0 c_p (T_0 - T_\infty)[W/m^2] \tag{2.27}$$

This equation is frequently used and the sensible heat flux is listed in Table 2.1. $T_\infty = 300K$ and is the ambient temperature, $\rho_\infty = 1.17 kg/m^3$, c_p is the specific heat of air at a constant pressure, A is the plume's cross-sectional area at the base. The cases listed in Table 2.1 fall under the intense fire range.

In the present study the power P is prescribed and, to study the Buoyancy Flux 2.25 influence on the plume, the inlet temperature is changed whilst maintaining the same velocity.

Chapter 3

Validation & Verification

Benchmark test cases were used to validate modeling assumptions selected to predict plumes in crossflow.

The first test is the velocity profile on a neutral ABL [29]. The second case is the plane jet in crossflow in a confined channel [30], and the third case is the Meteotron fire-plume experiment where the results are compared with the experiment, with the Fire Dynamics Simulator (FDS) and Clark coupled atmosphere-fire model [31]. In the first two test cases a URANS model was used to save computational resources, since the main focus was to guarantee the correct boundary conditions were being used. For the Meteotron fire plume, a verification and validation study was undertaken to derive adequate precautions in terms of grid resolution and accuracy of the modeling assumptions and to ensure the correct setup of the LES model.

3.1 Atmospheric Boundary Layer

The first validation case test is concerned to investigate if the solver used can correctly simulate a neutral Atmopheric Boundary Layer (ABL) profile. To achieve this, the data from [29] was used in order to compare the obtained results with already existing ones for an ABL evolution calculated using $RANS$. The turbulence model used in Yassin et. al. [29] calculations was the standard $k-\epsilon$ and the case was 2 Dimensional, while the data used to verify this present study was obtained using URANS in a 3 Dimensional domain. The turbulence model was kept the same as in [29] since there is no buoyancy involved in a neutral ABL and the expressions from [32] define the inlet profiles.

$$U(y) = \frac{u^*}{\kappa} ln\left(\frac{y-y_0}{y_0}\right) \tag{3.1}$$

$$k(y) = \frac{{u^*}^2}{\sqrt{C_\mu}} \tag{3.2}$$

$$\varepsilon(y) = \frac{{u^*}^3}{\kappa(y+y_0)} \tag{3.3}$$

where U is the mean streamwise velocity, $u* = 0.938 m/s$ is the friction velocity, κ is the Von Kármán constant (with $C_1 = 1.44$ and $C_2 = 1.92$) $\kappa = 0.4187$, y is the height from the ground [m], y_0 is the aerodynamic roughness [m] and $C_\mu = 0.09$ is a model constant.

The ABL friction velocity and Vón Karman constant are given by:

$$u^* = \frac{U_{ref}\kappa}{ln\left(\frac{y_{ref}+y_0}{y_0}\right)} \tag{3.4}$$

$$\kappa = \sqrt{\sigma_e(C_2 - C_1)\sqrt{C_\mu}} \tag{3.5}$$

The results present in Figure 3.1 show the comparison between the obtained vertical profiles of velocity U and turbulent kinetic energy k 500m downstream of the inlet and the data obtained from Yassin [29] as well as the initial imposed profiles. Overall the results are very satisfactory and support the model for the main results of the work which relates with plumes in an atmospheric boundary layer crossflow.

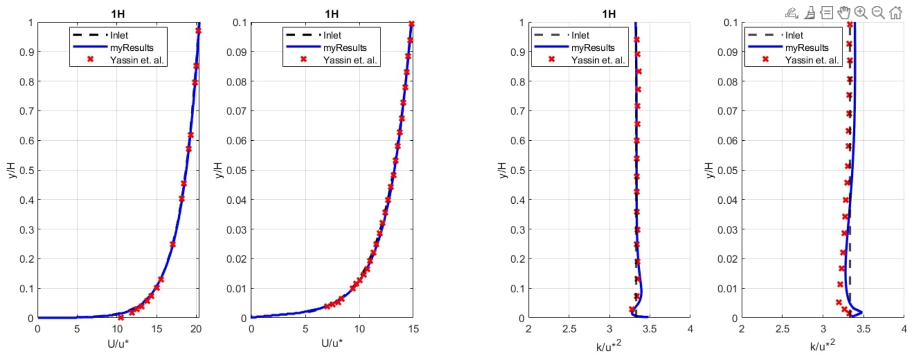

((a)) Velocity profiles **((b))** Turbulent kinetic energy profiles

Figure 3.1: Comparison of profiles between the present case (solid blue line), Yassin's case (red crosses) and the initial profiles (dashed black line)

3.2 Plane Jet in Crossflow

The second test used for the validation of the OpenFOAM model used is a plane jet discharged perpendicularly into a crossflow in a confined channel. Comparisons are made with Chen and Hwang's [33] experimental measurements and also with WP Jones and M. Wille's [30] numerical results with LES turbulence modeling.

The considered computational domain measurements were the same as the ones used by Chen and Hwang with a cross-section of $240 * 120mm^2$ and the inlet parameters were taken from [33] and a representation is presented in Figure 3.2.

The case chosen from ref. [33] was also studied and used for early LES simulations and validations by W.P. Jones. In this case the jet and crossflow velocities were given as $U_0 = 17.4m/s$ and $U_b = 2.37m/s$ with a momentum flux ratio of $J = 50.4$. In Jones's work he considered the flow to be isothermal because the temperature diference between jet and crossflow was negligible. However in the present case the temperatures used were the ones reported by Chen and Hwang ($T_0 = 315.05K$ and $T_\infty =$

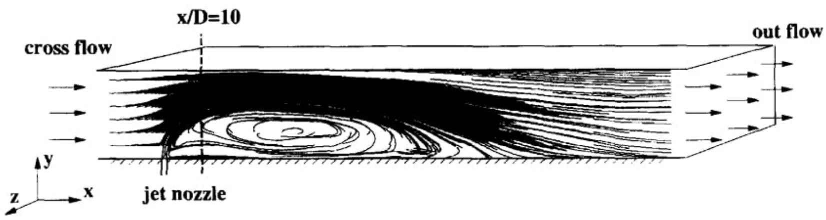

Figure 3.2: Illustrative figure of the flowfield taken from Ref. [30]

$296.65K$). Unfortunately the turbulent intensities were not provided for this experiment, and a value of $I = 0.05$ was assumed for both the jet and the crossflow.

The non-dimensional velocity used in [30] is described as

$$u_{\Theta} = \frac{u - u_{\infty}}{u_{max} - u_{\infty}} \tag{3.6}$$

where T and T_{max} are the local and the maximum local temperature at a distance x/D from the jet inlet, and u and u_{max} are the local and the maximum local streamwise velocity at the same distance.

As shown in Figure 3.3, the results obtained from the second case show reasonable agreement with the experimental measurements and with both the data reported by WP Jones and by Chen and Hwang.

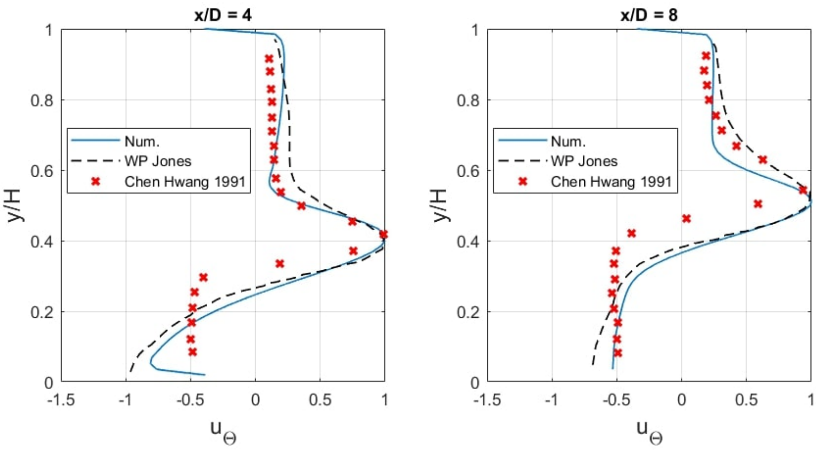

Figure 3.3: Plots of the non-dimensional velocity throughout the height of the channel for different distances from the jet inlet.

In this flow the plane jet is confined by the channel. This causes the jet to roll up into a large blob creating a hot recirculation region. The flow obtained is very similar to the one computed by Jones [30].

3.3 Meteotron Fire-Plume Experiment

From 1971 to 1973, several almospheric fire-plume experiments were carried out by Benech [34] using a $4000m^2$ hexagonal area filled with 97 oil burners that when ignited would produce a thermal power of around $600MW$ or $0.15MW/m^2$. The plume that was generated was then measured using various techniques such as by using kite balloons, photogrammetry, and radiosonde-radiowind systems. The boundaries of the plume were delimited by the presence of visible smoke. Up to heights of 600m above ground level (AGL) some of the plume properties were pretty much identical between experiments.

The Meteotron fire experiment was used by Sun et al. [31] as a benchmark to compare the plume properties obtained by the Fire Dynamics Simulator (FDS) and the Clark Coupled mildfire model. And these results are going to be used here to validate the plume generated by the FireFOAM solver, under LES turbulence modelling.

FDS uses a square fire of 63.25 x $63.25[m]$ with a heat release rate of $0.150MW/m^2$ with an isothermal atmosphere, while the Clark model uses a neutrally stratified atmosphere with a sensible heat flux source of $160kW/m^2$ over a slightly smaller area, so the total heat release comes out to the $600MW$ of the Meteotron fire. In the FireFOAM case, a hot jet was injected into the domain with a square inlet of $63.25m$. The fluid being injected into the domain is air and different temperatures were used in order to find out whether or not and to what extent it influenced the plume. The initial jet velocity was given in order to maintain the same heat-release rate (HRR) as in the Meteotron experiment. The atmosphere was isothermal as well, just like in the FDS simulation.

To match the domain used in R. Sun's work [31] a domain of 400 x 600 x $400[m]$ is going to be used and the grid used is an uniform mesh with around 1.3 million cells. This grid size is comparable to the FDS case where 1 million cells were used to simulate the plume generated by the Meteotron experiment.

3.3.1 Grid Independence study

To make sure that the grid used was fine enough, a separate study was performed where 2 extra mesh definitions were used. These will be called $Mesh1$, $Mesh2$ and $Mesh3$ and they have $20.7k$, $166k$ and $1.3M$ cells, respectively. Each mesh has a cell number ratio of $r = 8$ with the previous one.

To demonstrate the error decay with grid size, the mean vertical plume velocity at $y = 200m$ was compared between the different cases and the Grid Convergence Index (GCI) was calculated. In order to accomplish this, the Richardson extrapolation method was used in order to estimate the error's behavior with increase in mesh resolution. Since three meshes are available and the cell ratios between them are the same, the convergence ratio was obtained by

$$R = \frac{\phi_2 - \phi_1}{\phi_3 - \phi_2} \tag{3.7}$$

where ϕ is a generic integral quantity and the subscripts 1, 2 and 3 represent the solution in the fine, medium, and coarse meshes, respectively. As demonstrated in Table 3.1, the integral quantities used for this study were the mean, time averaged vertical velocity ($(u_y)_{plume}$) and temperature of the plume ($(T)_{plume}$) shown in Figure 3.4. For both these quantities, the error shows monotonic convergence because $0 < R < 1$ and the error falls under the asymptotic range. Therefore the GCI can be calculated by obtaining the observed order of accuracy p , and using it to get the GCI using the following expressions

$$p = \frac{ln\left(\frac{\phi_3 - \phi_2}{\phi_2 - \phi_1}\right)}{r} \tag{3.8}$$

$$GCI = F_s E_1 \tag{3.9}$$

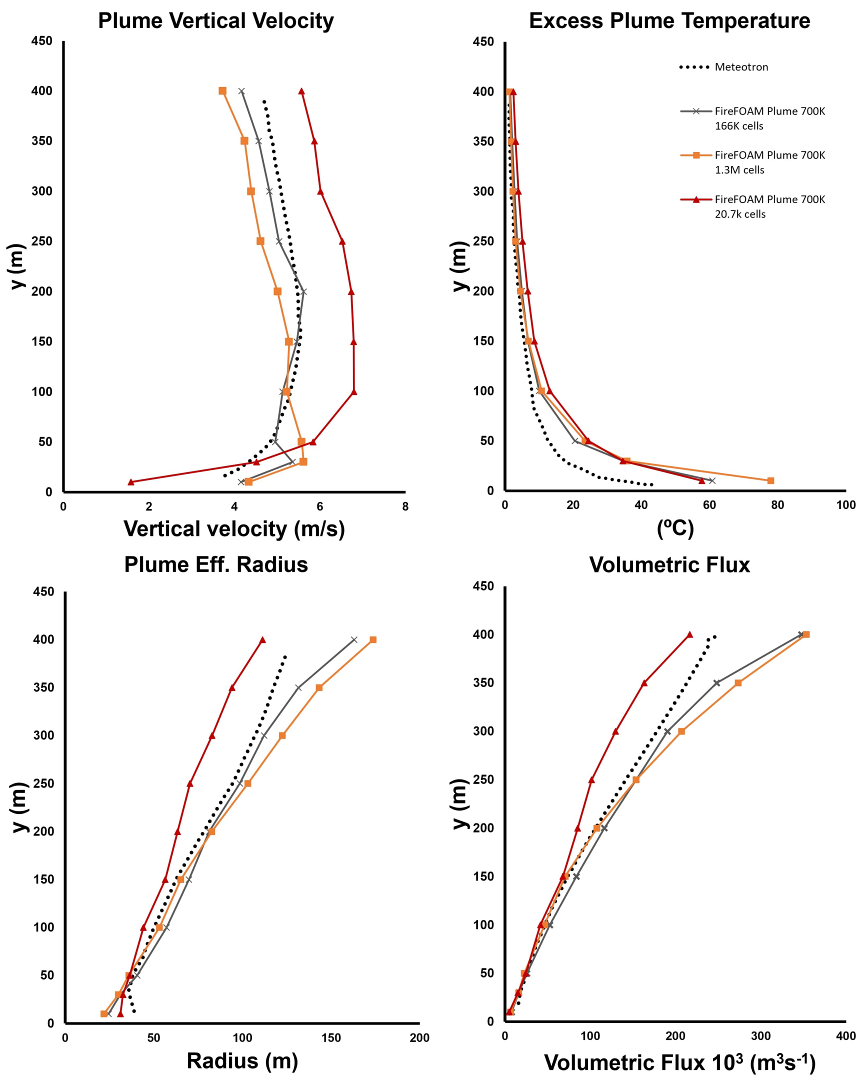

Figure 3.4: Different plume-averaged properties at different heights, as a function of mesh resolution.

$$E_1 = \frac{1 - \frac{\phi_2}{\phi_1}}{r^p - 1} \tag{3.10}$$

where r is the ratio between the medium grid spacing and the fine grid spacing and F_s is the safety factor, given the value of 1.25 because $1 < p < 2$ [35].

3.3.2 Results

To obtain the plume properties, the time-mean results were obtained employing the average procedure during $600s$. The plume averaged properties were obtained by the integration of the plume in several slices parallel to the ground.

In Figure 3.6 shows the comparison of the instantaneous plume cross-section obtained by FireFOAM and by Sun's FDS simulation and it illustrates good concordance between the two plumes, both having similar tilt angles and thickness. The tracer distribution in 3.6(a) shows a strong similarity with the soot distribution in 3.6(b).

The plume contour is obtained in the FDS calculation of soot density, but it is not easy to select a

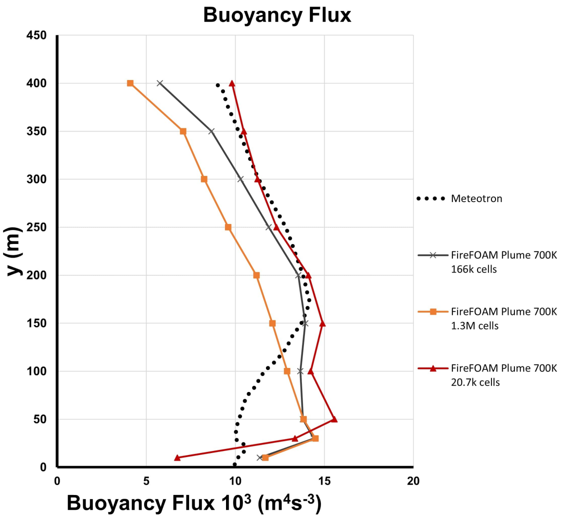

Figure 3.5: Plume-averaged buoyancy flux profiles for different mesh resolutions.

Table 3.1: Results of the grid independence study performed.

	$(u_y)_{Plume}$	$(T)_{plume}$
Mesh 1	9.07	309.30
Mesh 2	6.64	306.78
Mesh 3	6.31	306.62
R	0.13	0.065
p	1.45	1.97
GCI	0.0096	0.000046

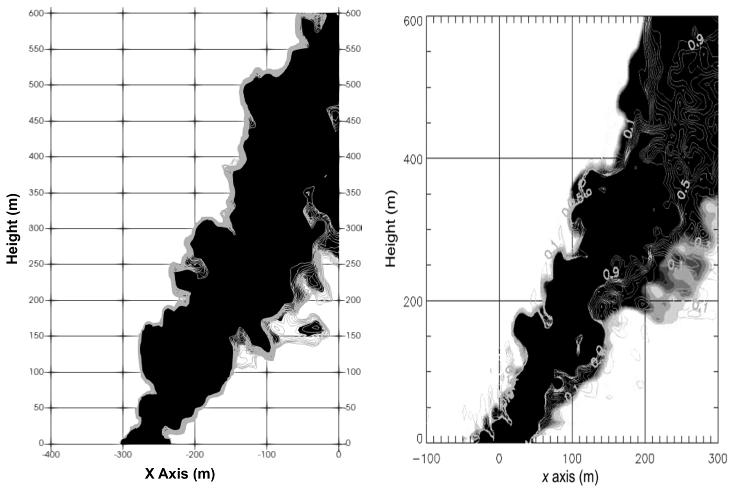

((a)) FireFOAM Plume tracer contours **((b))** FDS Plume soot contours

Figure 3.6: Side-by-side comparison between the present case plume (a)) and the smoke plume calculated by FDS (b), taken from [31]).

threshold of what is and what is not part of the plume. The Clark model does not contain a soot transport equation being solved. Therefore a different approach was used, based on the following parameter

$$\omega > \frac{\omega_{max}}{exp(c)} \tag{3.11}$$

where ω is the plume velocity normal to the ground, ω_{max} is the local maximum ground-normal velocity and c is an empirical constant with a suggested value of 1.38. This way every plume can be compared equally and the results can be comparable with each other without raising questions. Well defined instantaneous plume contours allow the plume properties to be calculated. The excess temperature of the plume, vertical velocity, effective radius, volumetric and buoyant fluxes were obtained for different buoyancy fluxes from the imposed jet temperatures that originate the lazy plumes.

Figure 3.7 shows the obtained results with the different inlet plume temperatures. For higher initial plume temperatures, the vertical velocity increases as a consequence of larger buoyancy. The plume's effective radius is also affected by the initial parameters, although not as much as the vertical velocity or the excess temperature. As for the Volumetric Flux, no clear tendency can be observed other than the FireFOAM plume having a curve that closely resembles the Meteotron experiment's data, in contrast to the FDS results. All of the parameters obtained from this study fit within a reasonable range of both the experimental and the numerical results obtained by Sun.

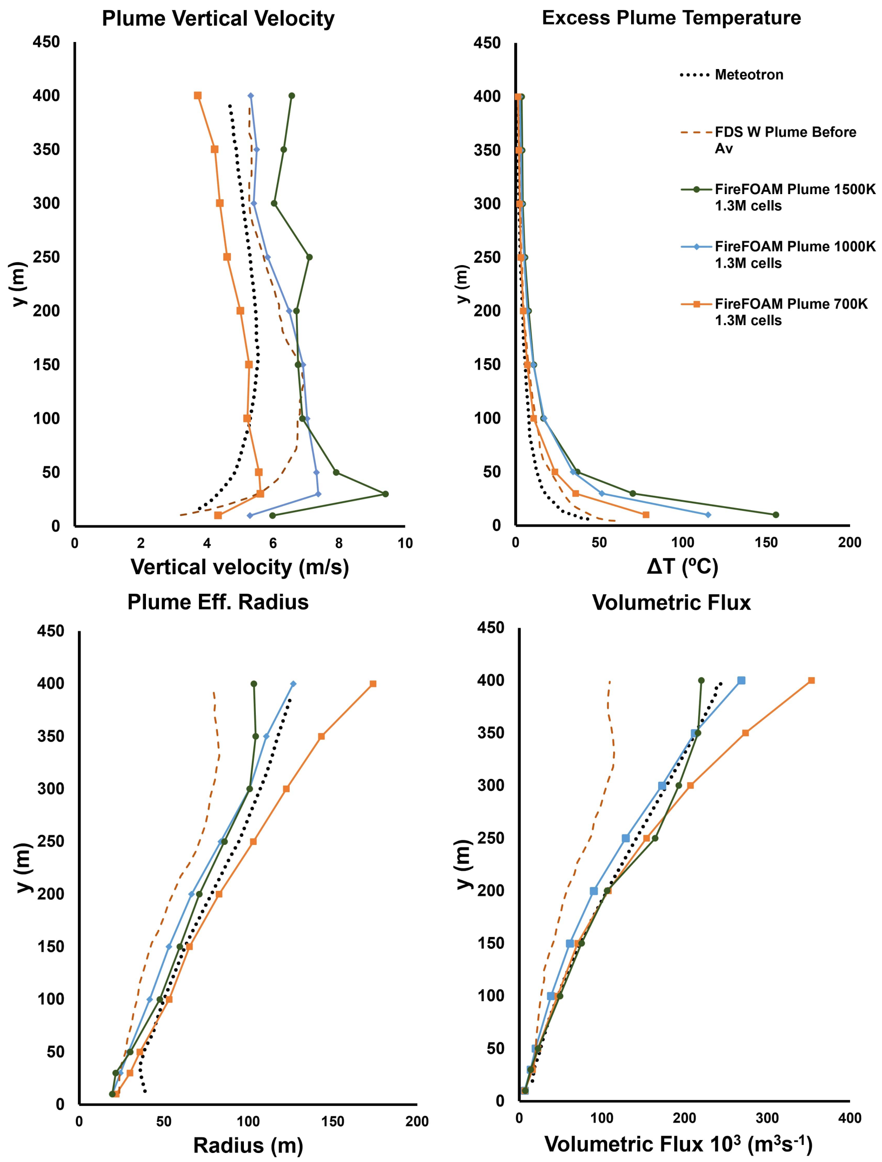

Figure 3.7: Comparison of different plume-averaged properties for plumes with different initial temperatures, with the Meteotron experiment and the FDS simulation

It becomes essential to make use of the Richardson number to check if the plume is momentum or buoyancy driven. In this case all of the plumes obtained through FireFOAM were buoyancy driven, but some had higher Buoyancy Fluxes than others. To make sure that the calculated plume matches the plume that it's being compared to, the buoyant fluxes must be very similar. Otherwise they are bound to be completely different. So with this in mind, the buoyant fluxes were calculated and as shown in Fig. 3.8, the 700K plume is the one that more accurately matches the experimental measurements.

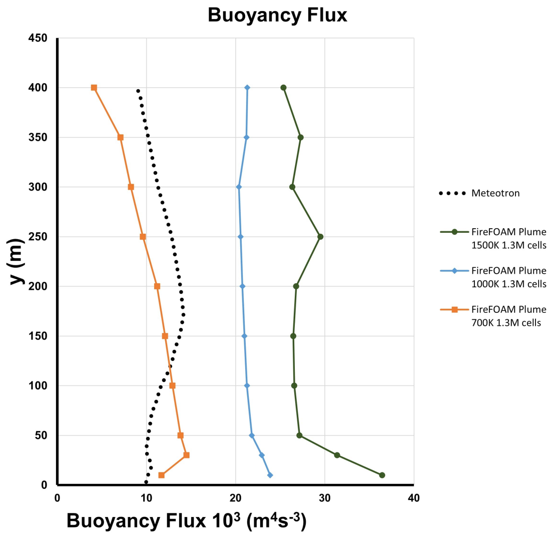

Figure 3.8: Comparison of the plume-averaged buoyancy flux profile of the different plumes with distinct initial temperatures and the Meteotron experiment.

With this it was concluded that the plume that more closely matched the Meteotron experiment was the one with an initial temperature of $T_0 = 700K$. Compared to the rest of the plumes, this is the one that, overall, better resembles the experimental data over the studied parameters.

Chapter 4

Results

4.1 Rectangular source plume in a crossflow

There is a fundamental difference between isothermic jets in a crossflow and hot plumes in crossflow, and that difference is the existence of a buoyant force acting on the plume, allowing it to reach greater heights over an extended distance. The positive buoyancy effect under crossflow is not constant in the cross-wind direction, and vanishes when the plume temperature tends asymptotically to the ambient temperature. For this reason, the plume rise varies differently with the distance from the inlet.

Along the plumes there are different regimes where different dynamics govern its behavior.

1. Momentum region: Where the plume motion is mainly driven by the initial momentum of the jet and the buoyancy has not yet affected its velocity greatly.

2. Buoyancy region: The buoyant forces start affecting the plume motion and accelerate it to higher vertical velocities (or lower ones in the case of negatively buoyant plumes)

3. Entrainment region: The plume is transported by the crossflow and ambient air is entrained into the plume in this region, turning its trajectory mainly horizontal and by the effect of the CRVP and other vortical structures.

For the entrainement region of the plume, where its motion is mostly horizontal, according to the semi-empirical equations from [36] [37], the jet and buoyant plume rises, z_j and z_{plume} respectively, are directly proportional to the distance from the inlet

$$z_j \propto x^{1/2} \tag{4.1}$$

$$z_{plume} \propto x^{2/3} \tag{4.2}$$

The calculations are firstly presented in the framework of unsteady flow fields, followed by a time-averaged analysis and finally the analysis of the effective plume. Each of these studies correspond to a subsection of the rectangular source plume calculations.

4.1.1 Unsteady Plume Structure

To investigate the influence of the buoyancy flux, four plumes have been considered, with buoyancy fluxes from 1633.3 to $52266.7 m^4/s^3$. In addition, three crossflow velocity ratios K are used for each of the buoyancy fluxes. Table 4.1 lists the relevant parameters for each of the 12 cases simulated, in which the buoyancy flux varies from approximately 1630 to $52000 m^4/s^3$. The subscript 0 refers to the initial plume injection properties and α is the thermal expansion coefficient and Table 4.2 lists the case nomenclature used in the description of the results.

Table 4.2 shows the nomenclature used for 12 different cases as a function of Fr and K.

Table 4.1: Detailed parameter description of the simulated plumes.

Case	K	$\rho_0(kg/m^3)$	$\alpha_0(*10^{-3}K)$	$Re_0 * 10^5$	J	$F_B(m^4/s^3)$	Fr	Ri	CPU Time (h)
1	0.5	1.01	1.14	24.3	0.292	1633.3	1.07	0.224	23.8
2	0.5	0.705	0.976	13.2	0.417	6533.3	0.68	0.766	36.6
3	0.5	0.353	0.670	4.25	0.834	22866.6	0.52	1.841	51.5
4	0.5	0.186	0.670	1.55	1.585	52266.7	0.48	4.209	60.1
5	1	1.01	1.14	24.3	1.167	1633.3	1.07	0.224	21.3
6	1	0.705	0.976	13.2	1.770	6533.3	0.68	0.766	31.0
7	1	0.353	0.670	4.25	3.335	22866.6	0.52	1.841	43.2
8	1	0.186	0.670	1.55	6.338	52266.7	0.48	4.209	49.8
9	2	1.01	1.14	24.3	4.666	1633.3	1.07	0.224	64.3
10	2	0.705	0.976	13.2	6.678	6533.3	0.68	0.766	73.5
11	2	0.353	0.670	4.25	13.341	22866.6	0.52	1.841	65.6
12	2	0.186	0.670	1.55	25.353	52266.7	0.48	4.209	77.0

Table 4.2: Different simulation cases

K/Fr	**1.07**	**0.68**	**0.52**	**0.48**
2	Case 1	Case 2	Case 3	Case 4
1	Case 5	Case 6	Case 7	Case 8
0.5	Case 9	Case 10	Case 11	Case 12

Varying these K and Fr parameters has shown a significant difference not only in plume height and trajectory, but also in smoke concentration, plume unsteadiness and bifurcation. Consequently, the the refinement boxes were iteratively placed onto the domain and refinement levels were tuned to meet the vorticity computation requirements of the LES turbulence modeling and ensure an accurate calculation. In cases where the plume rose to heights above the computational domain the dimensions were adjusted to fit the plume.

In this section we will mainly focus on the instantaneous structures and vortices generated by the interaction of the buoyant plume with the crossflow, and on analyzing the influence of the buoyancy flux on their frequency and strength.

Figures 4.1(a) and 4.1(b) shows the instantaneous Q-Criterion computation the cases 7 and 8, respectively. The invariant Q-Criterion of the velocity gradient tensor represents the balance between the rotation and strain rates. The Q isosurfaces are good indicators of coherent structures in a turbulent flow and is defined as

$$Q = \frac{1}{2}\left[(tr(\vec{U}))^2 - tr(\nabla\vec{U} \cdot \nabla\vec{U})\right] \tag{4.3}$$

The smoke emitted at the source follows a distinct path, more clearly seen in the time-averaged case, which will be discussed later. There are numerous instabilities affecting the smoke propagation. These instabilities are generated by vortices and vortical structures attached to the plume.

Buoyant jets in crossflow are very complex three-dimensional flows, that are characterized by the formation of different vortical structures. To better show some of these structures, Q-Criterion contours of a BJCF are shown in Figure 4.3(a) colormapped with the vertical component of vorticity, and the wake vortices are clearly visible underneath the counter-rotating vortex pair.

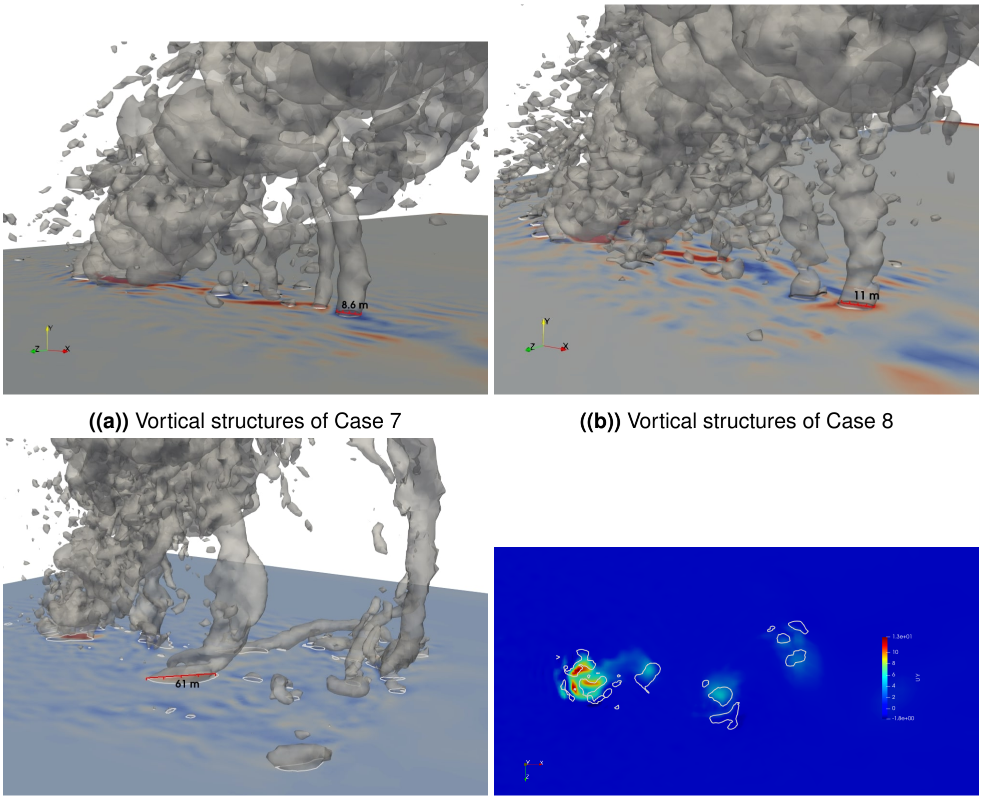

((a)) Vortical structures of Case 7

((b)) Vortical structures of Case 8

((c)) Vortical structures of the Meteotron plume

((d)) Vertical velocity slice at $y = 50m$.

Figure 4.1: Visualisation of the vortical structures, via $Q = 0.01$ isosurfaces, for different 4.1(a) Case 7, 4.1(b) Case 8, 4.1(c) Meteotron Case and 4.1(d) shows the vertical velocity close to the ground with white contours of $Q = 0.02$.

The wake vortices are stretched upwards and carry the air underneath towards the inside of the plume. However since there is no roll-up of the streamlines in these structures, they cannot be called upright vortices. In this case the WV are formed with alternating orientation but that may not always be the case, explained by Fric and Roshko in [3].

In the Meteotron case however, very strong upright vortices are formed underneath the plume, shown in 4.2(a) and 4.2(b). These structures are wider and stronger than the wake vortices seen before. With the use of ground level streamlines, it was possible to observe how the near ground flow behaves when interacting with these structures. The surrounding fluid is sucked up into the vortex and then shot up into the main body of the plume. Lagrangian particles were injected into the domain at 10m AGL and re-injected every time-step. As shown in Figure 4.2(c), the particles very closely follow the vortices up to distances of 700m and heights of 800m from the source. Which means that, if anywhere in this range, an ember is sucked up into these vortices while they are transporting flammable matter such as small dried up leaves or branches, it could possibly generate a fire whirl. These vortices are convected by the crossflow and travel throughout the domain. Because of this, they can not be seen in time averaged fields.They also lose strength as they travel. As these vortices travel downstream they get larger but weaker, and their entrainment diminishes as well. So the chance of this occurring further away from the source is smaller.

The maximum vertical velocity of the upright vortices was measured at a distance of 100m to 200m from the source and at 20m from the ground. The average of these velocities is presented in Table 4.3. The upright vortex maximum velocities scale inversely with the plume Froude number. The frequency at which these structures are generated was also measured by means of the non-dimensional Strouhal number $St = fD/u_\infty$. For the cases mentioned above, Table 4.3 shows that the Strouhal number slightly increases with the increase buoyancy flux and so does the frequency of generation of these vortices, which is in accordance with [6].

Table 4.3: The mean maximum vertical velocity of the upright vortices and their frequency for different plume buoyancy fluxes.

Cases	T_0 (K)	F_B (m^4/s^3)	$\overline{U_y}$ (m/s)	f (s^{-1})	St
Case 13	700	39 229.8	3.63	0.0139	0.299
Case 14	1000	68 652.2	2.12	0.0143	0.307
Case 15	1500	117 689.5	2.48	0.0152	0.326

Another vortical structure that is present in this flow is the counter-rotating vortex pair. These structures are more clearly seen in the time-averaged and they are not as clearly identifiable in the instantaneous field contours. The CRVP is the main structure of the jet in crossflow and the one that gives shape to the plume. Figure 4.3(b) shows the instantaneous vectors at a cross-plane on top of the plume's streamlines. The vectors show very clearly the effect of the CRVP in the flow. This structure, as the name implies, is formed by two identical vortices side by side with opposite orientations. These vortices may end up splitting the plume into two different branches where the smoke gets trapped inside of each of the vortices.

The analysis of the interaction between the shear layer Kelvin-Helmholtz vortices and the counter-rotating vortex pair cannot be analyzed in detail in the present simulations due to the need to a very finely refined mesh.

4.1.2 Time-averaged Plume Model

In this section, the time average of the instantaneous LES calculations is analyzed. Figure 4.5(a) shows the smoke concentration taken at the center of the time-averaged plume at different distances from the inlet, as demonstrated in 4.5(b). It should be mentioned that the wake vortices are time dependent structures that vanish in a time-averaged analysis. On the opposite, the counter-rotating vortex

((a)) $Q = 0.02$ isosurface of the Meteotron Plume, color-mapped with the vertical vorticity component.

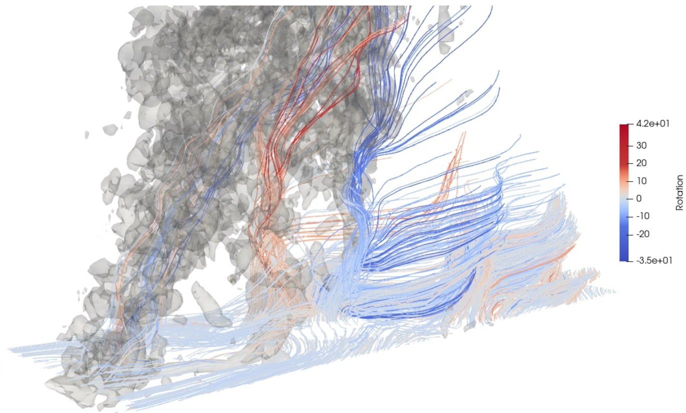

((b)) Streamline representation of the upright vortices in the Meteotron simulation.

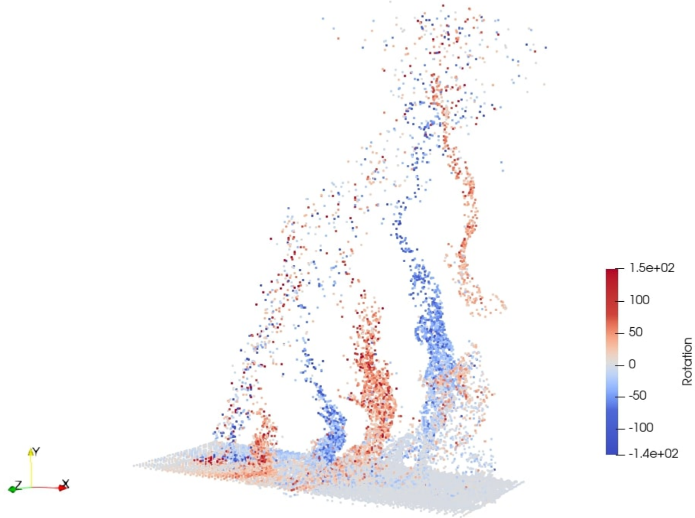

((c)) Trajectory of Lagrangian particles released 10m AGL.

Figure 4.2: $Q = 0.02$ isosurface prediction of the Meteotron Plume color-mapped with the vertical vorticity 4.2(a), streamline representation of the upright vortices 4.2(b) and trajectory of Lagrangian particles released at 10m AGL.

pair is the highlight in the time-averaged analysis, because during the unsteady process it is strongly deformed. Figure 4.4 shows the difference between the unsteady and a steady-state plume structure. In all cases, the peak of smoke concentration is coincident with these vortices (Figure 4.6).

Two important parameters to study the propagation of smoke are the plume expansion and the plume

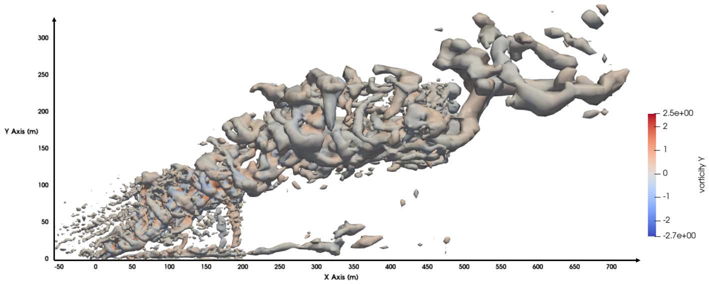

((a))

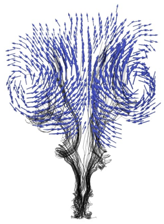

((b))

Figure 4.3: Case 8 $Q = 0.01$ a) isosurface and upstream view with flow streamlines and b) velocity vectors.

((a)) Instantaneous Plume

((b)) Time-averaged Plume

Figure 4.4: Side-by-side comparison between an instantaneous and time-averaged smoke plume, for $K = 1$ and $Fr = 0.52$.

tilt angle, θ and β respectively (see Figure 4.7), that describe how the plume grows and it's trajectory. The expansion angle is computed while the plume is still expanding and was taken at the cores of the counter-rotating vortices, and the tilt angle was taken as the initial angle that the plume makes with the ground.

The results are shown below in Table 4.4 and they show a very good correlation between θ with F and, although there are not quite enough points to establish a proportionality ratio between θ and K with a constant Froude number, there is clearly a decrease of θ with the decrease of K. And by combining K

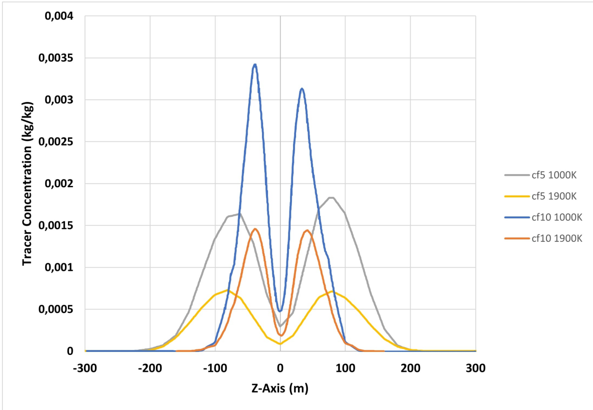

((a)) Cross-plume, time-averaged smoke concentration profiles for different plumes at $x/D = 60.2$

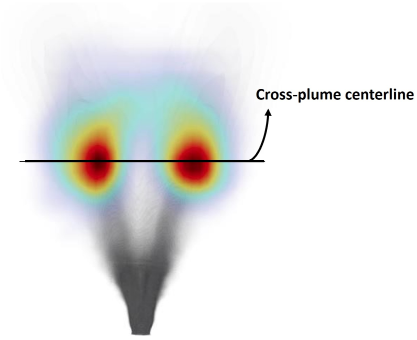

((b)) Cross-plume centerline representation.

Figure 4.5: Crossplume smoke concentration profiles.

and F it is possible to obtain an expression estimating the expansion angle of the plume by giving these two parameters as inputs, given in Eq. 4.4.

$$\theta = 5.1934 \left(\frac{Fr}{K}\right)^{-1.136} \tag{4.4}$$

Much like the expansion angle, a very good correlation was found that shows that this angle decreases with an increase of $\frac{Fr}{K}$, and is given by:

$$\beta = 25.204 \left(\frac{Fr}{K}\right)^{0.85} \tag{4.5}$$

as shown in Figure 4.8(b).

The results from these correlations show good agreement with the data obtained in this research, seen in Figure 4.8 a) and b), having a coefficient of determination of $r^2 = 0.8642$ and $r^2 = 0.9471$ for the expansion and tilt angles, respectively. This way one can estimate the area of smoke covered downstream of the wildfire up until the plume expansion eventually decreases and is simply carried away by the wind. Figure 4.8b) shows the tilt angle as a function of $\frac{Fr}{K}$ and the plume rise is depicted in Figure 4.9, also as a function of the ratio of the froude number and the velocity ratio. Consequently, for high Froude number values, the expansion and the tilt angles rise. Meaning that for higher buoyancy fluxes, the plume follows a more vertical trajectory and the lateral dispersion is also larger. With larger buoyancy fluxes, the plume rise increases and increasing the crossflow velocity has shown to have the opposite

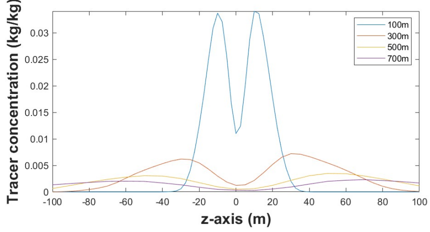

((a)) Case 7

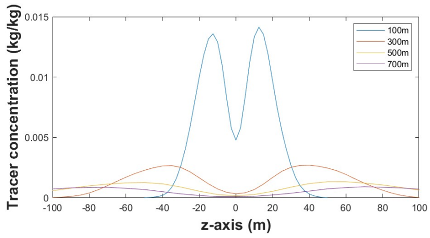

((b)) Case 8

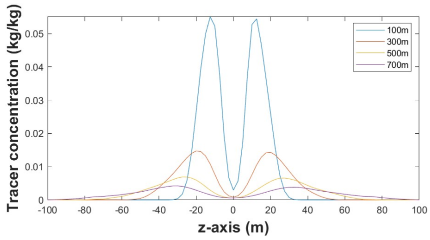

((c)) Case 11

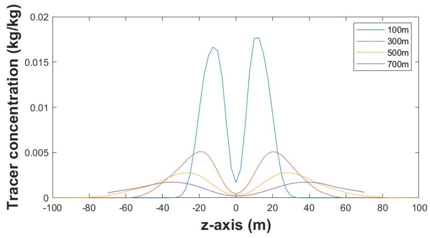

((d)) Case 12

Figure 4.6: Profiles of different cross-plume smoke concentrations (kg_{smoke}/kg_{mix}) at different distances from the source (a) 100m, (b) 300m, (c) 500m and (d) 700m

((a)) Expansion angle

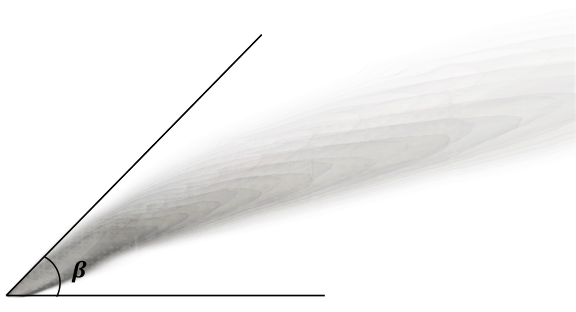

((b)) Tilt Angle

Figure 4.7: Representations of the expansion and tilt angles for the different plume cases.

effect.

Both the plume's Froude number and the velocity ratio affect the dispersion of smoke. Figure 4.8a) shows that for a higher Fr, the smoke dispersion is larger and lower concentrations of smoke are present in a larger area. The crossflow velocity however, has the opposite effect. The higher the crossflow

		Fr			
	$\theta(^\circ)$	**1.071**	**0.677**	**0.519**	**0.476**
k	**2**	10.77	19.12	31.84	21.64
	1	6.33	7.63	9.77	10.07
	0.5	1.99	4.23	3.83	4.36

Table 4.4: Plume expansion angles θ variation with K and Fr

velocity (lower K), the more concentrated the smoke becomes. Having a smaller dispersion in the atmosphere.

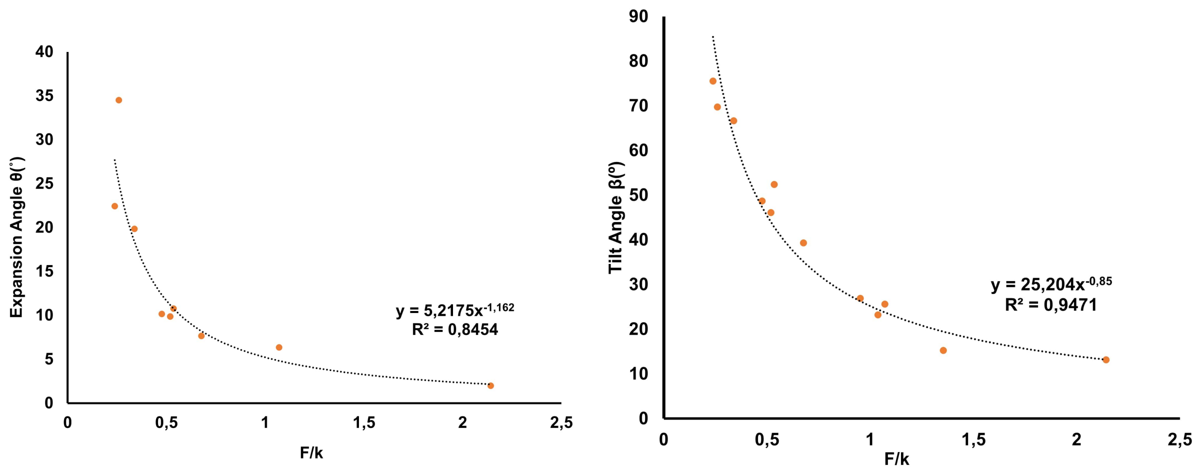

((a)) ((b))

Figure 4.8: Expansion angles 4.8(a) and tilt angles 4.8(b) for the different plume cases.

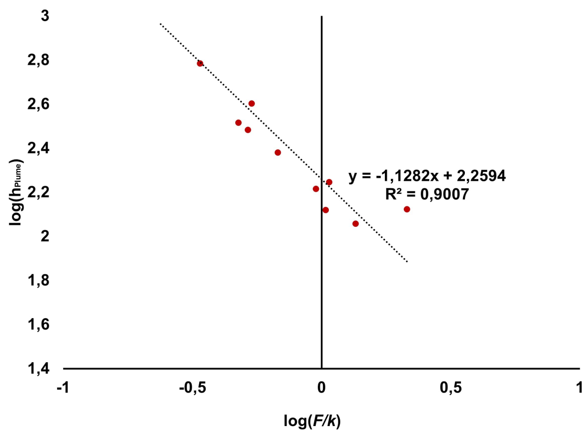

Figure 4.9: Plume rise of the different cases.

Figure 4.10 a) to f) shows the plume maximum values of temperature, vorticity and velocity, for the plumes with $K = 1$ and $K = 2$. It can be concluded from these plots that these quantities diminish with distance from the heat source. Also, by raising the buoyancy flux, the plume remains hotter for longer distances and the streamwise velocity remains somewhat constant along its path.

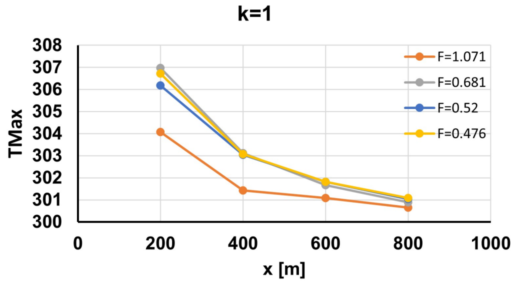

((a)) Maximum values of plume temperature, for cases 5, 6, 7 and 8.

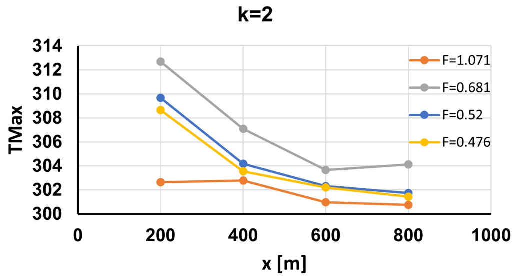

((b)) Maximum values of plume temperature, for cases 9, 10, 11 and 12.

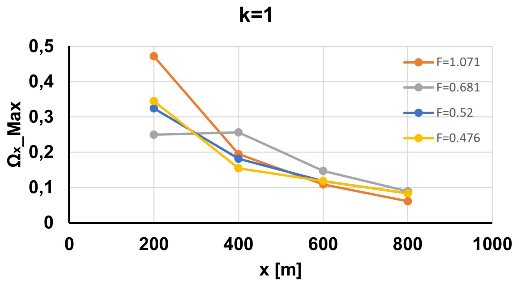

((c)) Maximum values of streamwise plume vorticity, for cases 5, 6, 7 and 8.

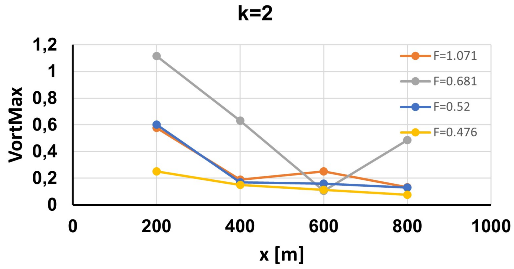

((d)) Maximum values of plume temperature, for cases 9, 10, 11 and 12.

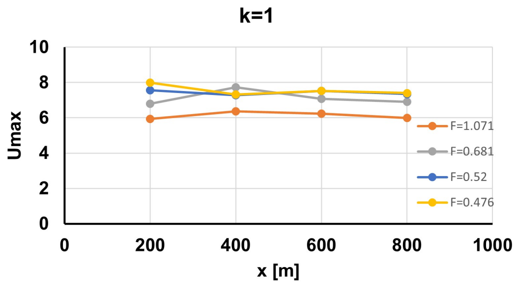

((e)) Maximum values of streamwise plume velocity, for cases 5, 6, 7 and 8.

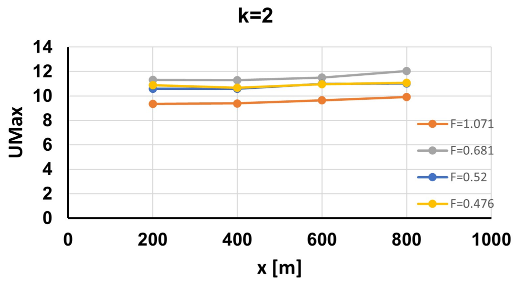

((f)) Maximum values of streamwise plume velocity, for cases 9, 10, 11 and 12.

Figure 4.10: Plots of maximum plume temperature, vorticity and velocity values at different distances from the source (200m, 400m, 600m and 800m).

4.1.3 Effective Plume Model

The effective plume model is obtained from an integral classic procedure that is used in engineering applications to investigate plumes. Consequently, there are no vortical structures present and the plume rise is calculated along a line, denominated of plume centerline. The classic theory allows for a satisfactory plume rise and concentration if the entrainment is well calibrated.

This method is used by meteorologists in mesoscale applications to predict the path of the contaminants present in plumes generated by wildfires. Usually this model is used when the domain of interest is in the scale of hundreds or even thousands of kilometers in the longitudinal direction and the fire intensity is such that the plume may be injected into the stratosphere. In these scenarios the near-field vortical structures are not of interest and the plume profile is assumed to have a Gaussian distribution. The classical plume theory gives the plume's asymptotic height and a Gaussian concentration profile to be included in the Mesoscale solvers as referred in the introduction section of this thesis.

From this point forward, unless stated otherwise,the only cases to be considered will be the cases 7, 8, 11 and 12. All of the cases with $K = 0.5$ will be discarded due to a very weak crossflow, not allowing the plume to bend over enough within the 1km computational domain length to take conclusions about the near far-field.

Once the smoke reaches this layer of the atmosphere it can be transported through very large distances and, when analyzing plume transport of this scale, meteorologists assume the smoke concentration is comparable to a gaussian distribution.

To calculate the effective plume, a cross wind integral (CWI) of the plume was performed at several heights and distances from the source. The results (Fig. 4.12) show the effective plume evolution as it's being transported downstream by the wind.

To verify whether or not this assumption is valid for this domain length, a comparison with the gaussian plume model concentration was performed. The smoke concentration was obtained through the expression 4.6 and is a function of the atmosphere's stability, crossflow velocity, contaminant emission rate and the the y and z axis.

$$C(x,y,z) = \frac{Q}{2\pi u_\infty \sigma_y \sigma_z} exp\left(\frac{y^2}{2\sigma_y^2}\right)\left[exp\left(-\frac{(z-H)^2}{2\sigma_z}\right) + exp\left(-\frac{(z+H)^2}{2\sigma_z^2}\right)\right] \tag{4.6}$$

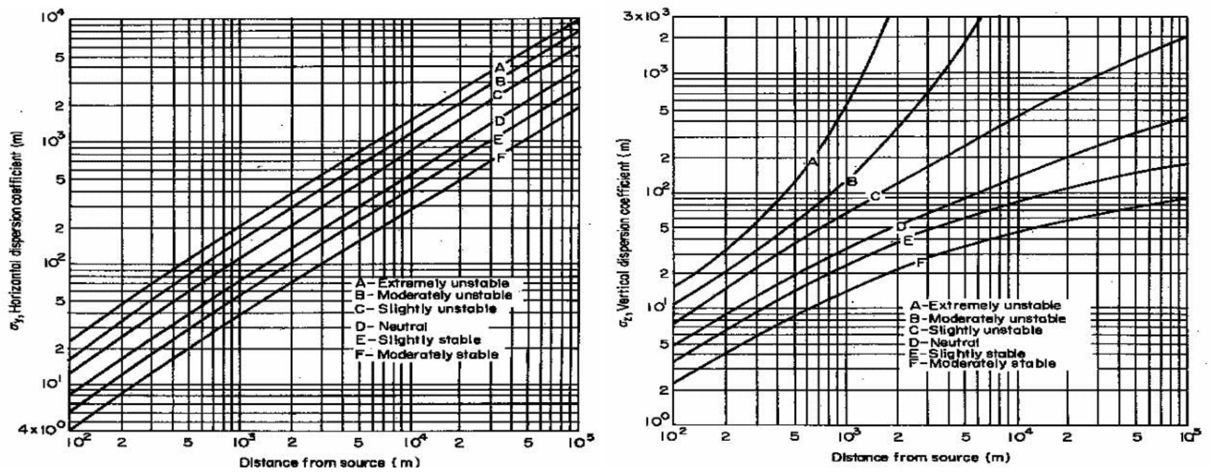

((a)) ((b))

Figure 4.11: Gaussian a) horizontal and b) vertical dispersion coefficient charts.

The σ_y and σ_z are the horizontal and vertical dispersion coefficients, respectively and H is the calculated plume rise the distance x from the source. These are a function of the atmosphere stability class and the distance from the source. The values used for these parameters were taken from the charts present in Figure 4.11 [38].

Figure 4.12 shows the different effective plume evolutions for cases 7, 8, 11 and 12 along the their path. And Figures 4.13, 4.14, 4.15 and 4.16 show the comparison between the effective plume concentration and the Gaussian plume profile for cases 7, 8, 11 and 12, respectively. The agreement is good for cases 7 and 8 and starts to deteriorate for the other cases. It is believed that the short distances, such as 200 and 400m from the plume source, the plume still presents strong curvature and the Gaussian plume model is not adequate.

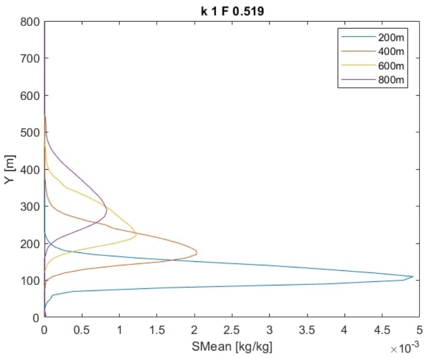

((a)) CWI profiles of Case 7

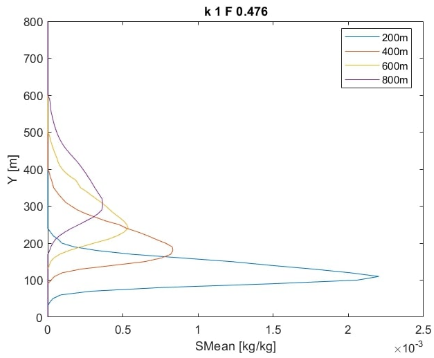

((b)) CWI profiles of Case 8

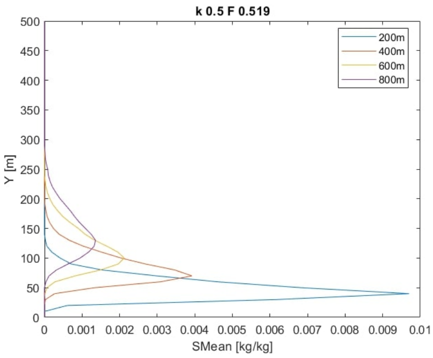

((c)) CWI profiles of Case 11

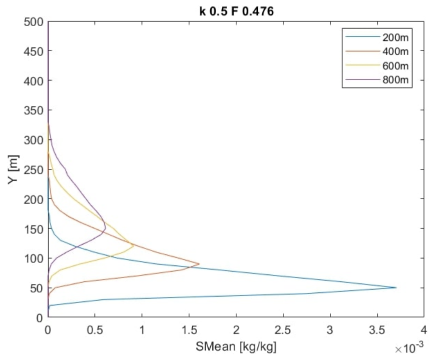

((d)) CWI profiles of Case 12

Figure 4.12: Effective Plume profiles for each relevant case, at different distances from the source (200m, 400m, 600m and 800m).

To study the trajectory of the plume centerline, the smoke concentration profiles were taken at several vertical slices throughout the domain. The local maximums of the concentrations dictate the centerline trajectory.

To study the trajectory of the plume the plume centerline by taking the maximum values of smoke concentrations in several slices throughout the domain and having those coordinates as the centerline points.

The important study of buoyant plumes published by G.A. Briggs for chemical chimney smoke propagation (Ref. [5]) shows a correlation for the plume trajectory in the transitional rise regime, given in Eq. 4.7. This is the regime when the plume first interacts with the crossflow and it is not strongly affected by stability due to its large initial momentum.

$$\Delta h = \frac{2F^{1/3}x^{2/3}}{\overline{u}} \tag{4.7}$$

$$F \approx g\frac{\Delta T}{T_0}\omega r^2 \tag{4.8}$$

where F in this case is a term proportional to the buoyancy flux, x is the downwind distance from the heat source, $\overline{u}$ is the average wind speed and g, ΔT is the temperature difference between the jet and the crossflow, ω is the jet velocity and r is the initial jet radius.

Another important aspect that can be obtained from Briggs' paper is the proportionality of the maxi-

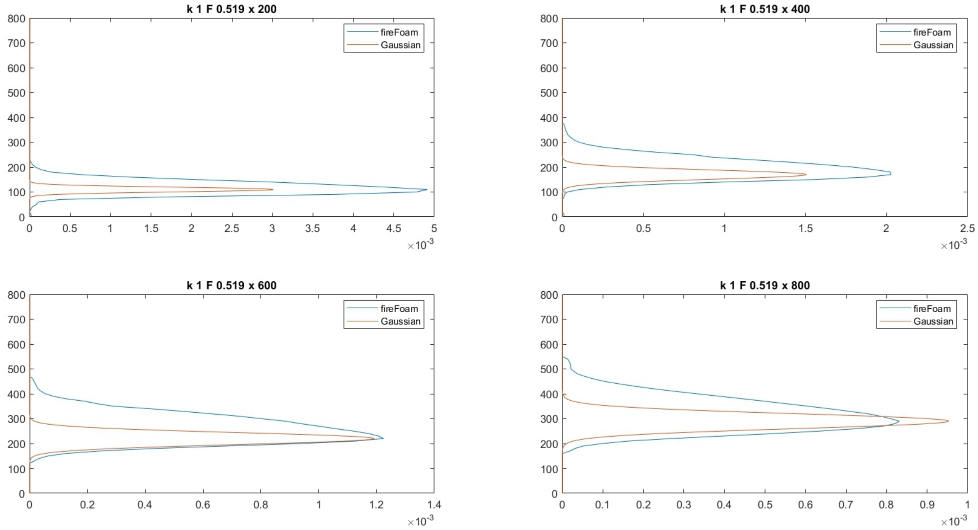

Figure 4.13: Comparison between the effective plume for Case 7 and the equivalent CWI Gaussian plume.

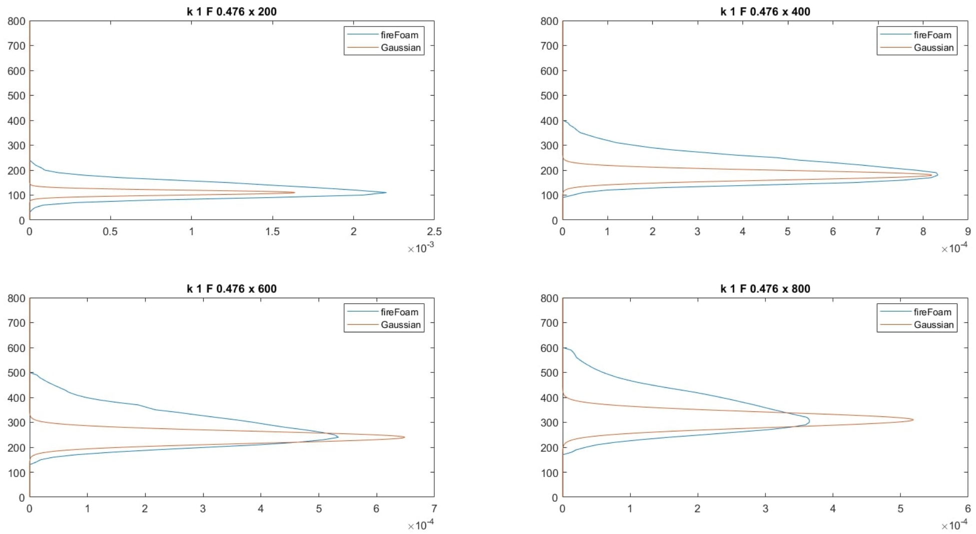

Figure 4.14: Comparison between the effective plume for Case 8 and the equivalent CWI Gaussian plume.

mum plume height to the ratio between the buoyancy flux and the wind velocity. Although this expression was initially proposed for fully developed plumes, as shown in Figure 4.17, it can also be used for plumes that have yet to stop raising in height. The plume heights were all taken at the end of the domain and show a similar trend when compared Briggs' plume rise values for the same plumes.

It is evident that the plume trajectory is affected by the parameters of the flowfield. As mentioned before, the parameters that were changed in the different cases were solely the Fr and K, but in nature there are numerous other parameters that affect the trajectory of the plume such as: wind turbulence, atmospheric stratification, ground roughness caused by the existence of trees buildings and/or vegetation, number and distance between heat sources, etc. Since it is not feasible to test all of these parameters, the priority was to study the Froude and K influence and hopefully other studies can show the plume

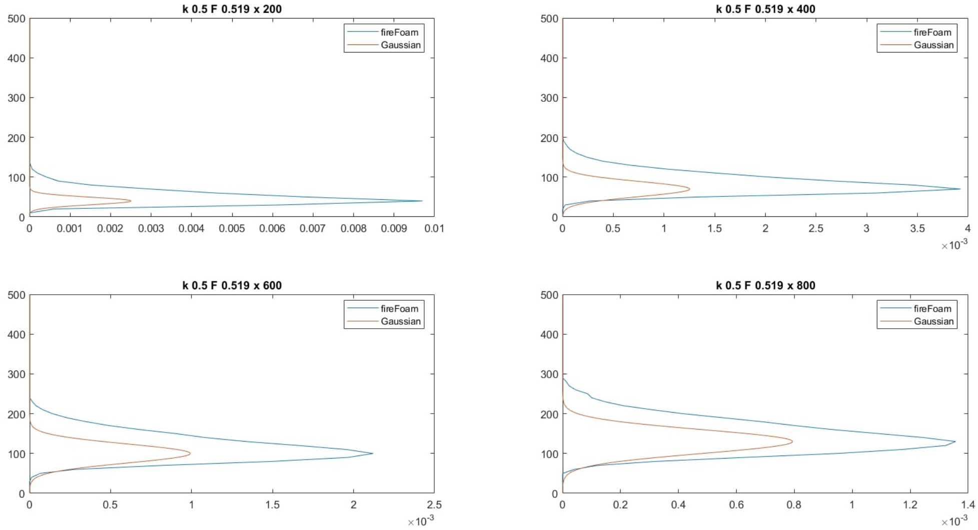

Figure 4.15: Comparison between the effective plume for Case 11 and the equivalent CWI Gaussian plume.

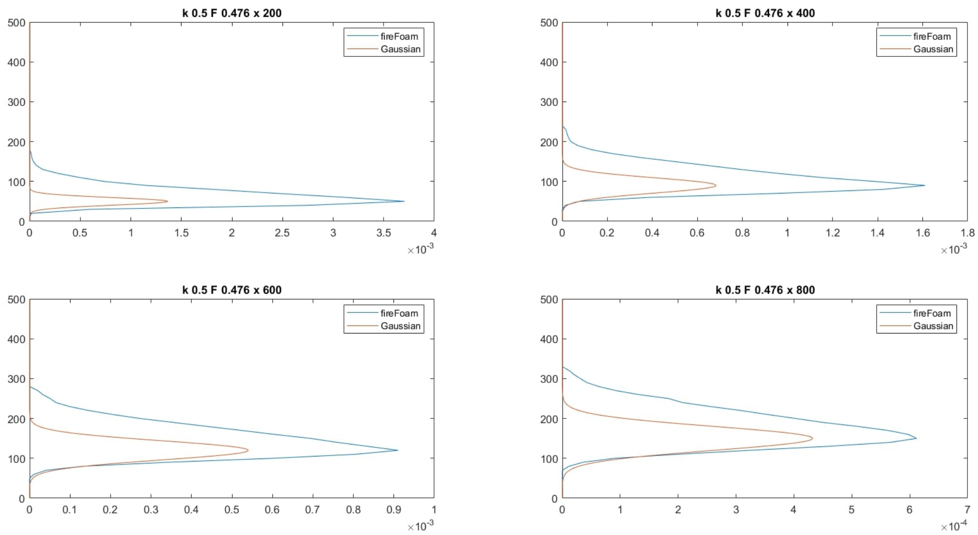

Figure 4.16: Comparison between the effective plume for Case 12 and the equivalent CWI Gaussian plume.

behavior as a function of other parameters.

4.2 Line Fire Plumes

The fronts of large or very intense wildfires may be spread as a continuous or semi-continuous line. Consequently, rectangular or spot fires, caused by the break-up of the line fires, and line fires are the dominant origin of fire plumes. The goal of the study presented in this section is to show how the source's geometry affects the plume structure and the formation of the counter rotating vortex pair, to better understand the influence of the aspect ratio of rectangular fires and to investigate of how the smoke from these fires is dispersed throughout the near-field surroundings.

For this study, two different setups were used. An infinite fire line was simulated using cyclic boundary

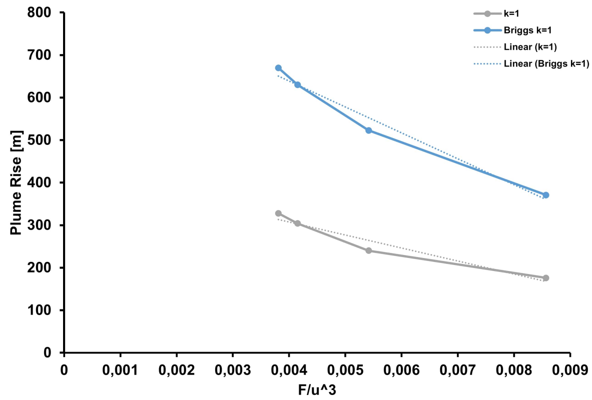

Figure 4.17: Calculated plume rise (solid grey line) comparison with Briggs's correlation (solid blue line) for cases 5, 6, 7, and 8.

conditions on the lateral boundaries. The heat-source length covered the whole domain so that when interacting with the perdiodic boundaries, it would simulate an infinite fire line. In the second setup, a long but finite fire line was considered, and pressure boundary conditions were used for the lateral boundaries. Figure 4.18 a) and b) show the three dimensional view with the nested arrangement and also the bottom surface mesh for the finite line-fire, respectively, and c) and d) show the same, but for the infinite line-fire.

Both of these cases were designed to have the same heat intensity per meter as the rectangular heat source cases. The same LES tubulence model used for the rectangular study was applied in both line fire cases. The crossflow velocity chosen was $10m/s$ and Table 4.5 lists a summary of the inlet parameters of the infinite and finite fire lines heat source analogy.

Case	Type	u_∞	$T_0(K)$	Fr	J	K	ρ_0	CPU Time (h)
Case 16	Infinite	10	1000	0.52	0.834	2	0.35	20.8
Case 17	Finite	10	500	0.68	0.417	2	0.71	58.7
Case 18	Finite	10	1000	0.52	0.834	2	0.35	47.8
Case 19	Finite	10	1900	0.48	1.585	2	0.19	54.6

Table 4.5: Summary of the inlet parameters for the line fire cases.

Figures 4.18(a) and 4.18(c) show a three dimensional view of the meshes used for the finite and infinite line fire cases, respectively. To get a better view of the inlet sections, Figures 4.18(b) and 4.18(d) show the finite and infinite case's bottom surface of the computational domain, respectively, with the plume inlet highlighted in red.

4.2.1 Unsteady line plume structure

The instantaneous structure of a line plume differs substantially from a rectangular plume because the counter-rotating vortex pair formation in the fire results from multiple longitudinal vortex structures. Figure 4.19(a) shows the formation of these vortices using three dimensional Q-criterion contours a finite line source (Case 19) and Figure 4.19(b) shows how the smoke follows these structures in the near region of the source.

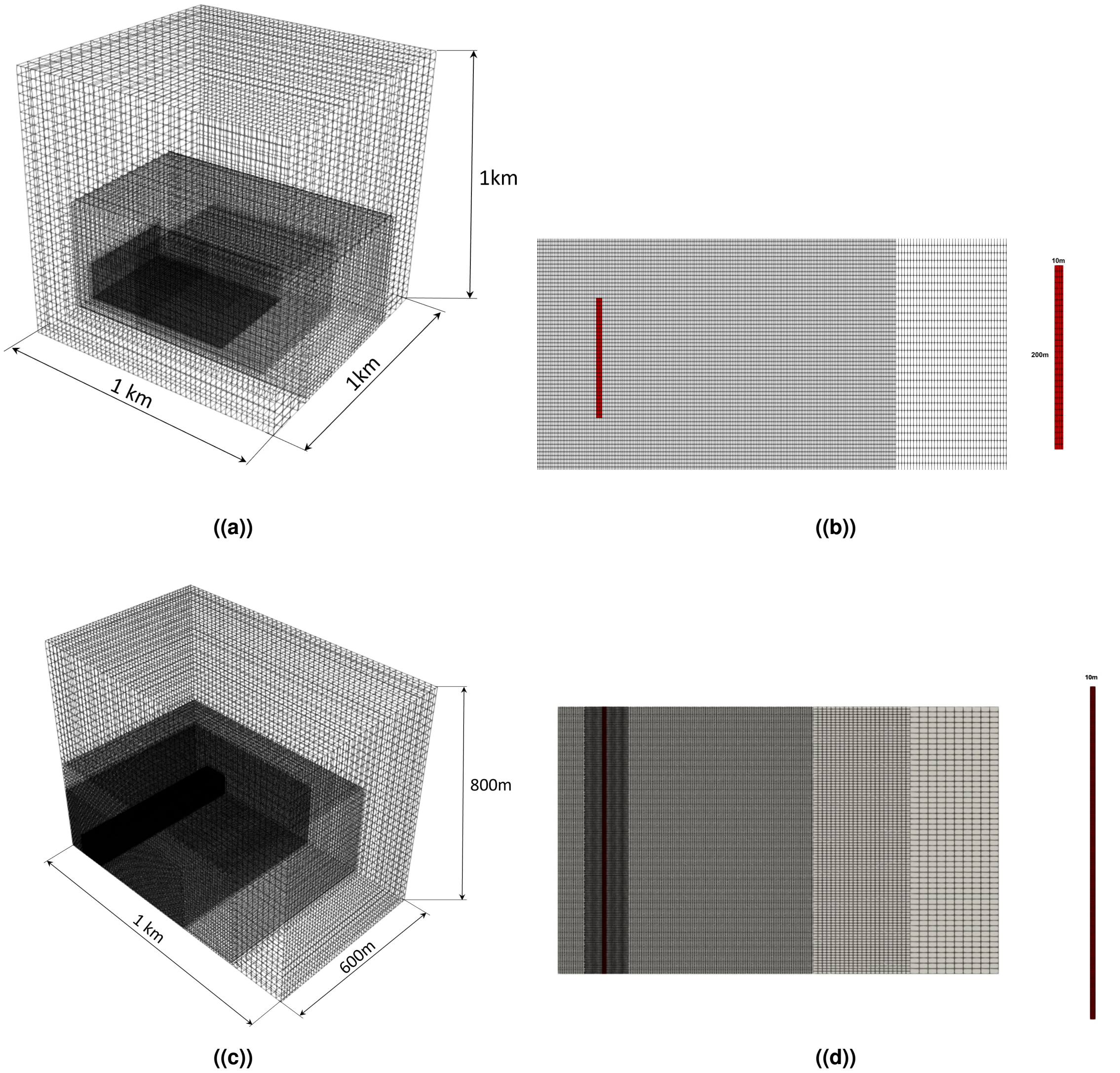

Figure 4.18: Computational domain of a) the Finite line-fire simulation 3D domain, b) close-up top-view of the heat source, c) computational domain of the infinite line fire case, d) close-u top-view of the infinite heat source.

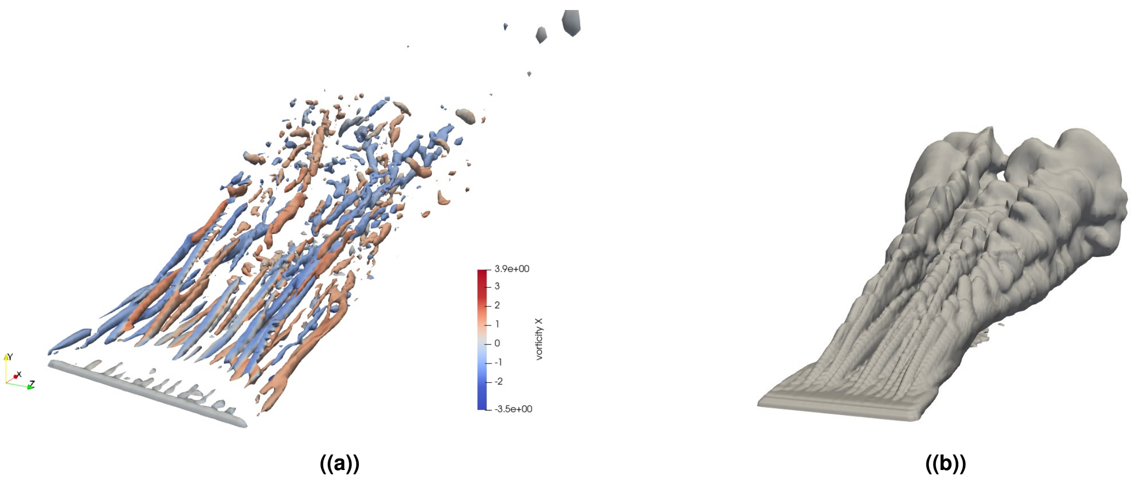

Figure 4.19: Instantaneous three-dimensional isosurfaces of a) $Q = 0.2$ and b) $\phi = 10^{-3}$ for case 19.

The line source fire induces, in the near region, the formation of multiple streamwise vortical structures as displayed in Figure 4.20(a) and denominated smoke streaks, visible by the generation of multiple vortex pairs. These , seen more closely in Figure 4.20(b), referenced by M. Finney [17], trap the smoke inside them and create streaks of smoke that interact with each among themselves and, far downstream, these structures generate the counter-rotating vortex pair.

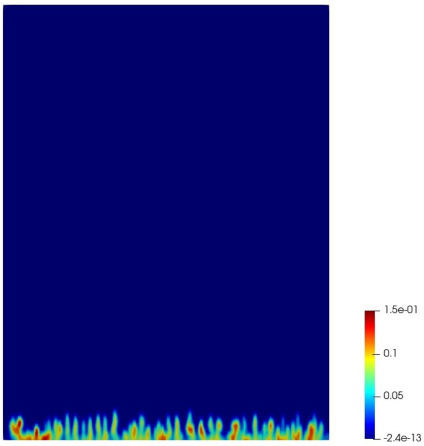

((a))

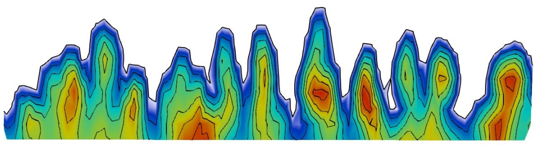

((b))

Figure 4.20: a) smoke concentration contours for Case 16 at $x = 150m$, where b) shows a zoomed up image of the concentration with line contours of the smoke concentration.

Finney [17] reported the wavelength of these vortices as a direct correlation to the flame length of the fire. In this case, as mentioned before, there is no fire. However, the flame length can be estimated by the heat release rate, in MW/m, being injected into the system. Therefore, using Equation 4.9, where L_t is the heat source's thickness, the equivalent line fire intensity is $17.5MW/m$. The intensity per meter of fire front is the same as in the rectangular source cases.

$$Q' = \rho_0 u_0 L_t c_p T_0 \tag{4.9}$$

The correlation given by Budnick [39] was used to estimate the flame length equivalent to a fire with the same intensity as the present case. This correlation is used to calculate the flame length of a line fire without crossflow. However, it was assumed to be a good enough estimate to the flame length with the crossflow. This correlation is given by

$$L_f = 0.017\dot{Q}'^{2/3} \tag{4.10}$$

Using this correlation, the approximate flame length of the present case is $L_f = 11.46m$. Now by the correlation given by Finney, we can obtain the approximate wavelength of the vortices

$$\lambda = 0.43L_f + 0.16 \tag{4.11}$$

This correlation gives an approximate vortex wavelength of $\lambda_{correlation} = 5.09m$.

In order to obtain the vortex wavelength of the present case, a streamwise vorticity plot was made just downstream of the source, see Figure 4.20. The number of structures seen in this plot was obtained and the measured vortex wavelength was around $\lambda_{exp} = 4.17m$. This value shows good accordance with the correlation given by Finney, as shown in 4.21, with a relative error of 18.1% calculated by Equation 4.12.

$$\epsilon = \frac{\lambda_{correlation} - \lambda_{exp}}{\lambda_{correlation}} \tag{4.12}$$

To analyze the influence of the lateral entrainment allowed by the finite plumes, and the effect of the buoyancy flux on these structures, the same procedure was made for cases 18 and 19. The results presented in Table 4.6 show that, for the same buoyancy flux as the case mentioned above, the results show even better agreement with the correlation given by Finney 4.11 with a relative error of 1.7% in case 18. For case 19 with the largest buoyancy flux it is seen that the size of these vortices increases, despite Q' and L_f remaining constant.

Table 4.6: Streak vortex wavelength for different cases.

Case	$T_0(K)$	$\lambda(m)$	$\epsilon(\%)$
16	1000	4.17	18.1
18	1000	5.18	1.7
19	1900	5.96	17.0

4.2.2 Time-Average Fire Line Plume

In the time-average field, the streak vortices mentioned earlier remain. Meaning that these structures are not transient and can remain in the same place, only oscillating up and down with the plume. Figure 4.22 shows the comparison of the time-averaged line source plume and the rectangular source plume. An interesting fact is that these vortices interact with each-other and, in the far field, the counter-rotating vortex, similar to the rectngular source plume, emerges.

Analyzing a little further downstream, in the finite line-source cases, the plume is convected downwind very close to the ground before it begins to rise. When the plume lifts off, a familiar plume structure begins to form, and analyzing the axial vorticity contours, it is evident that a counter-rotating vortex pair is once again generated.

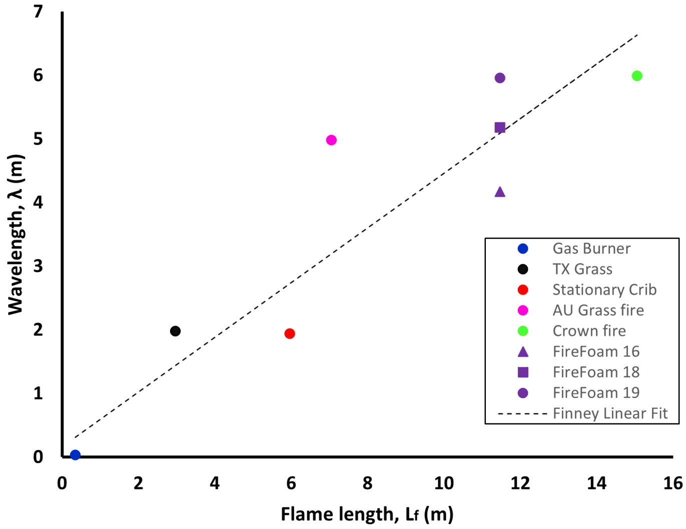

Figure 4.21: Comparison between the streak vortex wavelengths, as a function of wavelength, obtained by Finney in [17] and the ones calculated in cases 16, 18 and 19, depicted by purple triangle, square and dot, respectively.

For the finite line fire plume, the presence of the counter-rotating vortex pair is clear in the time-averaged field. However, because of the small length of the domain (1 km), in comparison to the length of the line source (200 m), the CRVP has not fully developed inside of the computational domain.

There is also a larger smoke concentration on the ground, especially in the near region of the plume. This may be caused due to the lack of lateral entrainment to the middle section of the plume, preventing it from rising up imediately downstream of the source.

When comparing the line-source plumes to the lower aspect-ratio ones, with the same crossflow velocity and buoyancy flux, it is observed that despite the line-source smoke plume being much more dispersed and covering much more area than the previous, the plume rise is similar between the two. This is an interesting phenomenon thay happens because of the buoyancy flux imediatly after the line source release. The heat from the source is transfered into the crossflos more intensively on the source's edges rather than at the middle of the finite line heat source.

Figure 4.23 shows the vorticity contours for the cases 17, 18 and 19 at different distances from the source. In the first case, the counter-rotating vortex appears in the middle of the line-fire and is convected downstream, interacting with the other stuctures along its path, resulting in the formation of a larger counter-rotating vortex pair at the end of the computational domain. For the other two cases, the near-source region is formed by multiple vortical structures (the streak vortices) that, similarly to case 17, interact with each-other and merge into one single counter-rotating vortex pair. The structure at the end of the computational domain is seen in Figure 4.24 and the contours show the smoke plume profile follows the trend of the spot-fire smoke plume, with two peaks inside of the vortices.

4.2.3 Effective Plume Model

The applied procedure was the same as the one outlined in section 4.1.3 to obtain the effective plume from integration of the 3D time-averaged data. The main interest is to quantify the average concentration

Figure 4.22: Time-average line fire and rectangular plume smoke contour comparison with $K = 2$ and $Fr = 0.478$.

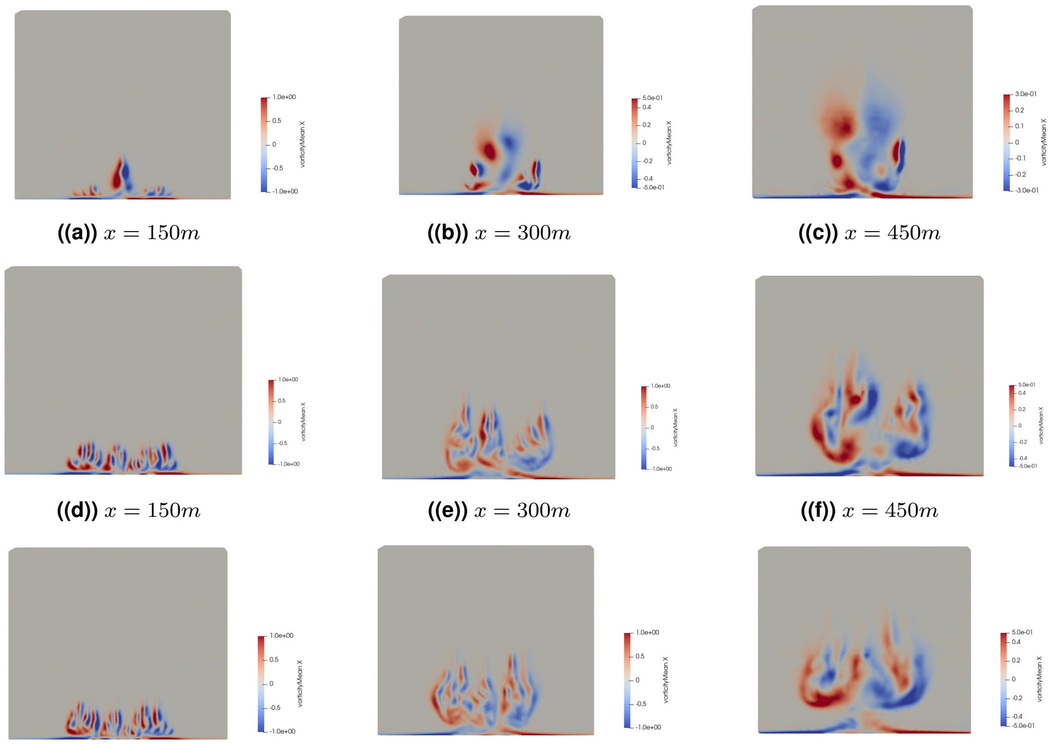

((a)) $x = 150m$ **((b))** $x = 300m$ **((c))** $x = 450m$

((d)) $x = 150m$ **((e))** $x = 300m$ **((f))** $x = 450m$

((g)) $x = 150m$ **((h))** $x = 300m$ **((i))** $x = 450m$

Figure 4.23: Time-average streamwise vorticity contours for different distances from the source and 400m span for: case 17 a), b) and c); case 18 d), e) and f); case 19 g), h) and i).

value and to compare with a single gaussian plume distribution.

Figures 4.25 and 4.26 show the concentration profiles of the effective plumes for the infinite and finite line fire plumes, respectively, at different distances from the source.

The ground smoke concentration is very high when compared to the rectangular heat source. This

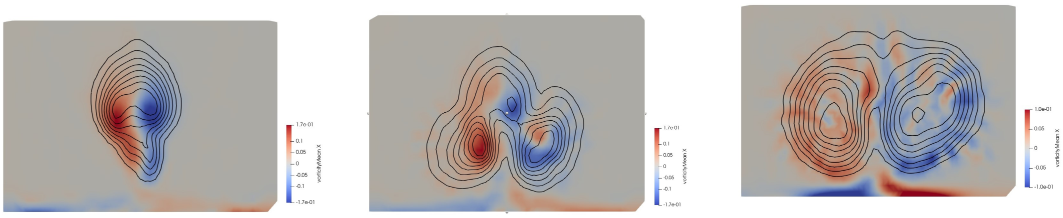

((a)) Case 17 ((b)) Case 18 ((c)) Case 19

Figure 4.24: Streamwise vorticity slices at $x = 900m$ with $700m$ span and smoke concentration contours.

effect occurs in the finite line fires, in the near region of the source, despite the open lateral boundaries. This is because in the source's very near region, the high length of the line fire makes very difficult for air to be naturally entrained in this region. Therefore, the very near-field, can be closely represented by an infinite line fire.

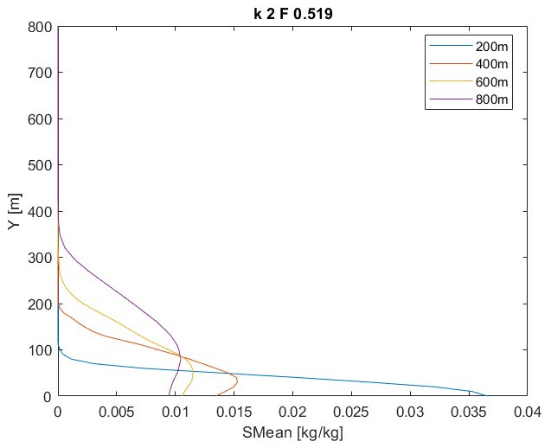

Figure 4.25: Effective plume smoke concentration (kg/kg) profile for the infinite line fire (Case 16).

For the Gaussian plume model prediction, as seen in Figure 4.27 the same trend from the rectangular fire plumes applies. The Gaussian plume model has better correspondence with the effective plume for larger distances from the source.

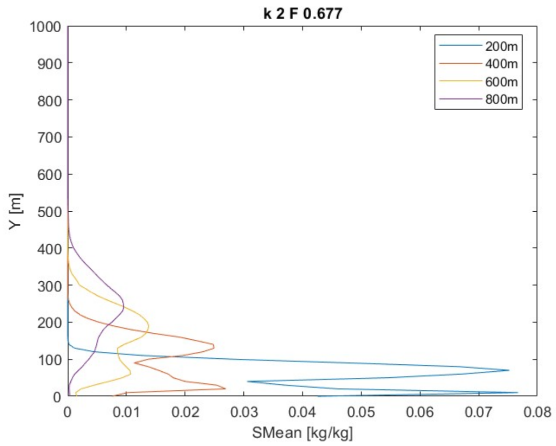

((a))

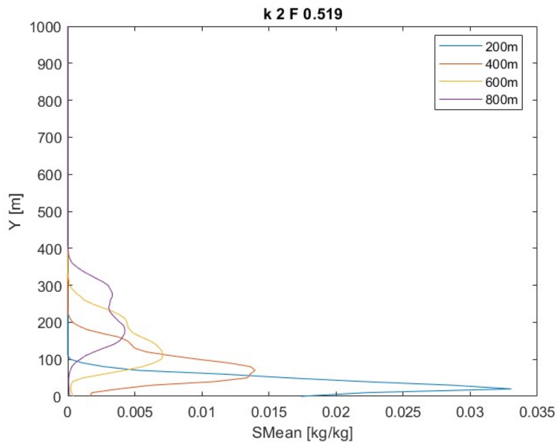

((b))

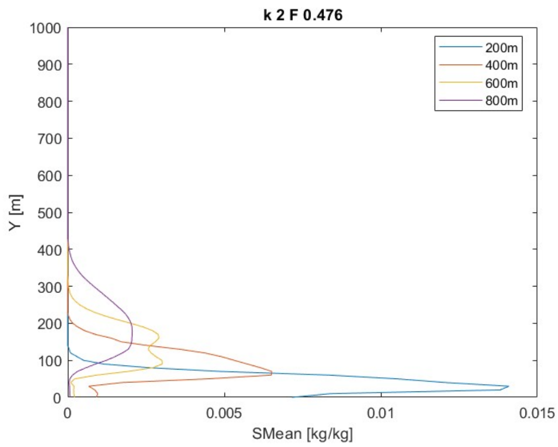

((c))

Figure 4.26: Effective plume smoke concentration (kg_{smoke}/kg_{mix}) for Case 17 (4.26(a)), Case 18 (4.26(b)) and Case 19 (4.26(c)) at $x = 200m$, $x = 400m$, $x = 600m$ and $x = 800m$.

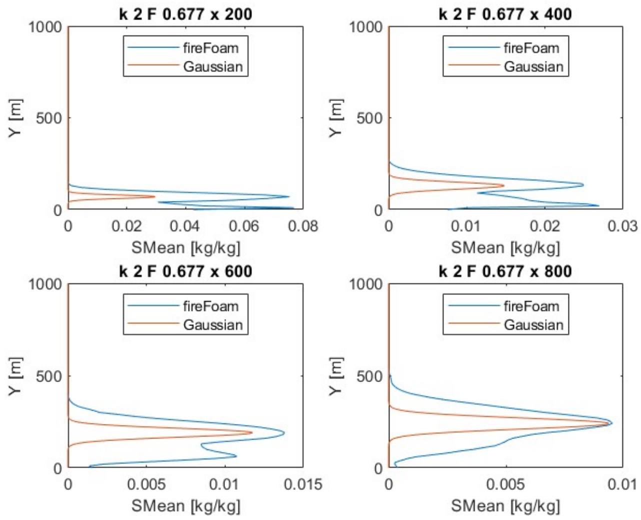

((a)) Effective plume concentration comparison with the gaussian model plume for the case 17 at $200m$, $400m$, $600m$ and $800m$ from the source.

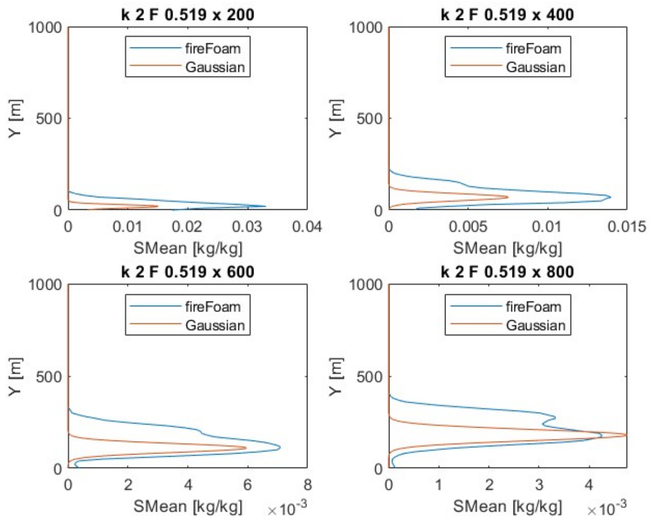

((b)) Effective plume concentration comparison with the gaussian model plume for case 18 at $200m$, $400m$, $600m$ and $800m$ from the source.

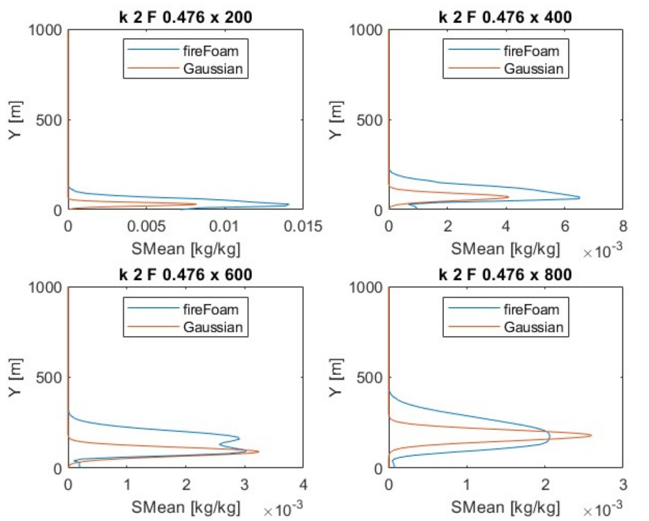

((c)) Effective plume concentration comparison with the gaussian model plume for case 19 with $Fr = 0.48$ at $200m$, $400m$, $600m$ and $800m$ from the source.

Figure 4.27: Effective plume concentration comparison with the gaussian model plume for 4.27(a) case 17, 4.27(b) case 18 and 4.27(c) case 19 at $200m$, $400m$, $600m$ and $800m$ from the source.

Chapter 5

Conclusions

In this work, the effect of the buoyancy flux, crossflow velocity and geometry of the source on the behavior of a smoke plume was studied.

The code used was verified and a validation was successfully performed by comparing the results of the numerical simulation with experimental measurements of a smoke plume in crossflow, capturing the wide array of unsteady vortical structures present in the flow.

5.1 Low aspect-ratio sources

For low aspect-ratio plume sources, the wake and upright vortices increase in strength and radius with an increase of the buoyancy flux. Their formation frequency is also higher for larger buoyancy fluxes. Upright vortices need a higher intensity plume to be generated, when compared to wake vortices. These structures transport matter from the ground into the plume, potentially generating fire-whirls. They lose strength as they are transported downwind of the source.

A time average of the plumes was then made, in order to better quantify the changes between cases and was found that for higher buoyancy fluxes, the plume velocities and vorticity are higher. Not only that, but the area covered by the smoke after 900m is larger. The crossflow velocity has the opposite effect, causing the plume to have larger smoke concentrations over a smaller area for larger wind speeds.

A cross-wind integral of the plumes was made, in order to get a better understanding of the effective smoke profile and compare it to the Gaussian plume model profile. The results were satisfactory, given that the conditions at which this integration was made was not the recommended since the plume has not yet reached its asymptotic height.

5.2 High aspect-ratio sources

For high aspect-ratio sources the plume geometry and vortex system is very different than low aspect-ratio plumes, especially in the near region. The longitudinal streak vortices grow in size with increase of buoyancy flux. The interaction of the longitudinal vortices, along with lateral entrainment, generates a counter-rotating vortex pair. These plumes also show a higher smoke concentration at the ground level near the source, due to the lack of lateral entrainment to the central region as a consequence of the high aspect ratio.

5.3 Future Work

The near region of the plumes is a very complex and chaotic region, with several different interactions between multiple vortical structures. It is very difficult to obtain plume correlations for this region due to the lack of consistent and universal behavior. More effort and studies must be conducted to this region of plumes in crossflow in order to have a better understanding of the dynamics of the vortex system and the generation of the vortical structures present.

Bibliography

[1] S. R. Freitas, K. M. Longo, R. Chatfield, D. Latham, M. A. F. Silva Dias, M. O. Andreae, E. Prins, J. C. Santos, R. Gielow, and J. A. Carvalho Jr. Including the sub-grid scale plume rise of vegetation fires in low resolution atmospheric transport models. *Atmospheric Chemistry and Physics*, 7(13):3385–3398, 2007. doi: 10.5194/acp-7-3385-2007. URL `https://acp.copernicus.org/articles/7/3385/2007/`.

[2] S. R. Freitas, K. M. Longo, J. Trentmann, and D. Latham. Technical note: Sensitivity of 1-d smoke plume rise models to the inclusion of environmental wind drag. *Atmospheric Chemistry and Physics*, 10(2):585–594, 2010. doi: 10.5194/acp-10-585-2010. URL `https://acp.copernicus.org/articles/10/585/2010/`.

[3] T. F. Fric and A. Roshko. Vortical structure in the wake of a transverse jet. *Journal of Fluid Mechanics*, 279:1–47, 1994. doi: 10.1017/S0022112094003800.

[4] R. M. Kelso, T. T. Lim, and A. E. Perry. An experimental study of round jets in cross-flow. *Journal of Fluid Mechanics*, 306:111–144, 1996. doi: 10.1017/S0022112096001255.

[5] G. A. Briggs. A plume rise model compared with observations. *Journal of the Air Pollution Control Association*, 15(9):433–438, 1965. doi: 10.1080/00022470.1965.10468404.

[6] Z. M. Moussa, J. W. Trischka, and S. Eskinazi. The near field in the mixing of a round jet with a cross-stream. *Journal of Fluid Mechanics*, 80(1):49–80, 1977. doi: 10.1017/S0022112077001530.

[7] G. Ernst, J. Davis, and S. Sparks. Bifurcation of volcanic plumes in a crosswind. *Bulletin of Volcanology*, 56:159–169, 08 1994. doi: 10.1007/BF00279601.

[8] Natural aerodynamics. By R. S. Scorer. London (Pergamon Press), 1958. Pp. xi, 312; Figs; Tables; 22 Plates. 60s. *Quarterly Journal of the Royal Meteorological Society*, 84(362):480–480, Oct. 1958. doi: 10.1002/qj.49708436231.

[9] J. S. Turner. A comparison between buoyant vortex rings and vortex pairs. *Journal of Fluid Mechanics*, 7(3):419–432, 1960. doi: 10.1017/S0022112060000189.

[10] T. Hayashi. Bifurcation of bent-over plumes in the ocean. *Coastal Engineering in Japan*, 15(1):153–165, 1972. doi: 10.1080/05785634.1972.11924155. URL `https://doi.org/10.1080/05785634.1972.11924155`.

[11] Y. Lv, H. Wei, T. Liu, X. Zhao, Y. Liu, B. Huang, and G. Wang. Numerical investigation of the round jet in crossflow at high velocity ratios with special emphasis on the evolution of vortex structures. *Physics of Fluids*, 34(3):034116, 03 2022. ISSN 1070-6631. doi: 10.1063/5.0084275. URL https://doi.org/10.1063/5.0084275.

[12] P. Huq and M. R. Dhanak. The bifurcation of circular jets in crossflow. *Physics of Fluids*, 8(3): 754–763, 03 1996. ISSN 1070-6631. doi: 10.1063/1.868859. URL https://doi.org/10.1063/1.868859.

[13] H. Baum, K. McGrattan, and R. Rehm. Simulation of smoke plumes from large pool fires. *Symposium (International) on Combustion*, 25(1):1463–1469, 1994. ISSN 0082-0784. doi: https://doi.org/10.1016/S0082-0784(06)80790-3. URL https://www.sciencedirect.com/science/article/pii/S0082078406807903. Twenty-Fifth Symposium (International) on Combustion.

[14] J. Trelles, K. B. McGrattan, and H. R. Baum. Smoke dispersion from multiple fire plumes. *AIAA Journal*, 37(12):1588–1601, 1999. doi: 10.2514/2.659. URL https://doi.org/10.2514/2.659.

[15] D. A. Haines and M. C. Smith. Three types of horizontal vortices observed in wildland mass and crown fires. *Journal of Applied Meteorology and Climatology*, 26(12):1624 – 1637, 1987. doi: 10.1175/1520-0450(1987)026⟨1624:TTOHVO⟩2.0.CO;2. URL https://journals.ametsoc.org/view/journals/apme/26/12/1520-0450_1987_026_1624_ttohvo_2_0_co_2.xml.

[16] C. R. Church, J. T. Snow, and J. Dessens. Intense atmospheric vortices associated with a 1000 mw fire. *Bulletin of the American Meteorological Society*, 61(7):682 – 694, 1980. doi: 10.1175/1520-0477(1980)061⟨0682:IAVAWA⟩2.0.CO;2. URL https://journals.ametsoc.org/view/journals/bams/61/7/1520-0477_1980_061_0682_iavawa_2_0_co_2.xml.

[17] M. A. Finney, J. D. Cohen, J. M. Forthofer, S. S. McAllister, M. J. Gollner, D. J. Gorham, K. Saito, N. K. Akafuah, B. A. Adam, and J. D. English. Role of buoyant flame dynamics in wildfire spread. *Proceedings of the National Academy of Sciences*, 112(32):9833–9838, 2015. doi: 10.1073/pnas.1504498112. URL https://www.pnas.org/doi/abs/10.1073/pnas.1504498112.

[18] N. Frangieh, G. Accary, D. Morvan, S. Méradji, and O. Bessonov. Wildfires front dynamics: 3d structures and intensity at small and large scales. *Combustion and Flame*, 211:54–67, 2020. ISSN 0010-2180. doi: https://doi.org/10.1016/j.combustflame.2019.09.017. URL https://www.sciencedirect.com/science/article/pii/S0010218019304316.

[19] A. Yoshizawa. Statistical theory for compressible turbulent shear flows, with the application to subgrid modeling. *The Physics of Fluids*, 29(7):2152–2164, 07 1986. ISSN 0031-9171. doi: 10.1063/1.865552. URL https://doi.org/10.1063/1.865552.

[20] H. G. Weller, G. Tabor, H. Jasak, and C. Fureby. A tensorial approach to computational continuum mechanics using object-oriented techniques. *Computers in physics*, 12(6):620–631, 1998.

[21] R. Issa. Solution of the implicitly discretised fluid flow equations by operator-splitting. *Journal of Computational Physics*, 62(1):40–65, 1986. ISSN 0021-9991. doi: https://doi.org/10.1016/0021-9991(86)90099-9. URL https://www.sciencedirect.com/science/article/pii/0021999186900999.

[22] R. Issa. Solution of the implicitly discretised fluid flow equations by operator-splitting. *Journal of Computational Physics*, 62(1):40–65, 1986. ISSN 0021-9991. doi: https://doi.org/10.1016/0021-9991(86)90099-9. URL https://www.sciencedirect.com/science/article/pii/0021999186900999.

[23] D. Viegas, C. Ribeiro, M. Almeida, P. Pinto, L. Ribeiro, and Silva. Field and laboratory analysis of the junction fire process in the catastrophic fire of pedrógão grande in june 2017. *International Journal of Wildland Fire*, 05 2023. doi: 10.1071/WF22161.

[24] M. Almeida, L. Ribeiro, J. Raposo, M. Viegas, R. Oliveira, D. Alves, C. Pinto, H. Jorge, A. Rodrigues, D. Lucas, D. Viegas, S. Lopes, and L. Silva. O complexo de incêndios de pedrógão grande e concelhos limítrofes, iniciado a 17 de junho de 2017. 10 2017.

[25] L.-N. Fan. Turbulent buoyant jets into stratified or flowing ambient fluids. 1967.

[26] B. R. Morton. Forced plumes. *Journal of Fluid Mechanics*, 5(1):151–163, 1959. doi: 10.1017/S002211205900012X.

[27] G. R. HUNT and N. B. KAYE. Lazy plumes. *Journal of Fluid Mechanics*, 533:329–338, 2005. doi: 10.1017/S002211200500457X.

[28] D. X. Viegas. *Convective Processes in Forest Fires*, pages 401–420. Springer Netherlands, Dordrecht, 1998. ISBN 978-94-011-5058-3. doi: 10.1007/978-94-011-5058-3_17. URL https://doi.org/10.1007/978-94-011-5058-3_17.

[29] Y. Toparlar, B. Blocken, B. Maiheu, and G. van Heijst. Cfd simulation of the near-neutral atmospheric boundary layer: New temperature inlet profile consistent with wall functions. *Journal of Wind Engineering and Industrial Aerodynamics*, 191:91–102, 2019. ISSN 0167-6105. doi: https://doi.org/10.1016/j.jweia.2019.05.016. URL https://www.sciencedirect.com/science/article/pii/S016761051930131X.

[30] W. Jones and M. Wille. Large-eddy simulation of a plane jet in a cross-flow. *International Journal of Heat and Fluid Flow*, 17(3):296–306, 1996. ISSN 0142-727X. doi: https://doi.org/10.1016/0142-727X(96)00045-8. URL https://www.sciencedirect.com/science/article/pii/0142727X96000458.

[31] R. Sun, M. A. Jenkins, S. K. Krueger, W. Mell, and J. J. Charney. An evaluation of fire-plume properties simulated with the fire dynamics simulator (fds) and the clark coupled wildfire model. *Canadian Journal of Forest Research*, 36(11):2894–2908, 2006. doi: 10.1139/x06-138. URL https://doi.org/10.1139/x06-138.

[32] P. RICHARDS and R. HOXEY. Appropriate boundary conditions for computational wind engineering models using the k- turbulence model. In S. Murakami, editor, *Computational Wind Engineering 1*, pages 145–153. Elsevier, Oxford, 1993. ISBN 978-0-444-81688-7. doi: https://doi.org/10.1016/B978-0-444-81688-7.50018-8. URL https://www.sciencedirect.com/science/article/pii/B9780444816887500188.

[33] K. Chen and J. Hwang. Experimental study on the mixing of one-and dual-line heated jets with a cold crossflow in a confined channel. *AIAA journal*, 29(3):353–360, 1991.

[34] B. Benech. Experimental study of an artificial convective plume initiated from the ground. *Journal of Applied Meteorology and Climatology*, 15(2):127 – 137, 1976. doi: 10.1175/1520-0450(1976)015⟨0127:ESOAAC⟩2.0.CO;2. URL https://journals.ametsoc.org/view/journals/apme/15/2/1520-0450_1976_015_0127_esoaac_2_0_co_2.xml.

[35] L. Eça and M. Hoekstra. Discretization uncertainty estimation based on a least squares version of the grid convergence index. 01 2006.

[36] J. H.-w. Lee and V. H. Chu. *Turbulent jets and plumes: a Lagrangian approach*, volume 1. Springer Science & Business Media, 2003.

[37] B. R. Morton, G. I. Taylor, and J. S. Turner. Turbulent gravitational convection from maintained and instantaneous sources. *Proceedings of the Royal Society of London. Series A. Mathematical and Physical Sciences*, 234(1196):1–23, 1956. doi: 10.1098/rspa.1956.0011. URL https://royalsocietypublishing.org/doi/abs/10.1098/rspa.1956.0011.

[38] M. Beychok. *Fundamentals of Stack Gas Dispersion*. 01 2005. ISBN 0-9644588-0-2.

[39] E. Budnick, D. Evans, and H. Nelson. Simplified fire growth calculations. (18th Edition), 1997-12-31 1997. URL https://tsapps.nist.gov/publication/get_pdf.cfm?pub_id=861184.

Appendix A

List of Detailed Boundary Conditions

```
/*--------------------------------*- C++ -*----------------------------------*\
| =========                 |                                                 |
| \\      /  F ield         | OpenFOAM: The Open Source CFD Toolbox           |
|  \\    /   O peration     | Version:  4.x                                   |
|   \\  /    A nd           | Web:      www.OpenFOAM.org                      |
|    \\/     M anipulation  |                                                 |
\*---------------------------------------------------------------------------*/
FoamFile
{
    version     2.0;
    format      ascii;
    class       volVectorField;
    location    "0";
    object      U;
}
// * * * * * * * * * * * * * * * * * * * * * * * * * * * * * * * * * * * * * //

dimensions      [0 1 -1 0 0 0 0];

internalField   uniform (0 0 0);

boundaryField
{
    "(outlet|sides)"
    {
        type            pressureInletOutletVelocity;
        value           uniform (0 0 0);
    }

    base
    {
        type            noSlip;
    }

    inlet
    {
        type            fixedValue;
        value           uniform (0 5 0);
    }

    wind
    {
        type            fixedValue;//pressureInletOutletVelocity;
        value           uniform (5 0 0);
    }
}


// ************************************************************************* //
```

Figure A.1: Velocity boundary conditions.

```
/*--------------------------------*- C++ -*----------------------------------*\
| =========                 |                                                 |
| \\      /  F ield         | OpenFOAM: The Open Source CFD Toolbox           |
|  \\    /   O peration     | Version:  4.x                                   |
|   \\  /    A nd           | Web:      www.OpenFOAM.org                      |
|    \\/     M anipulation  |                                                 |
\*---------------------------------------------------------------------------*/
FoamFile
{
    version     2.0;
    format      ascii;
    class       volScalarField;
    location    "0";
    object      T;
}
// * * * * * * * * * * * * * * * * * * * * * * * * * * * * * * * * * * * * * //

dimensions      [0 0 0 1 0 0 0];

internalField   uniform 300;

boundaryField
{
    "(outlet|sides)"
    {
        type            inletOutlet;
        inletValue      $internalField;
        value           $internalField;
    }

    base
    {
        type            zeroGradient;
    }

    inlet
    {
        type            fixedValue;
        value           uniform 1000;
    }

    wind
    {
        type            fixedValue;
        value           $internalField;
    }
}


// ************************************************************************* //
```

Figure A.2: Temperature boundary conditions.

```
/*--------------------------------*- C++ -*----------------------------------*\
| =========                 |                                                 |
| \\      /  F ield         | OpenFOAM: The Open Source CFD Toolbox           |
|  \\    /   O peration     | Version:  dev                                   |
|   \\  /    A nd           | Web:      www.OpenFOAM.org                      |
|    \\/     M anipulation  |                                                 |
\*---------------------------------------------------------------------------*/
FoamFile
{
    version     2.0;
    format      binary;
    class       volScalarField;
    location    "0";
    object      s;
}
// * * * * * * * * * * * * * * * * * * * * * * * * * * * * * * * * * * * * //

dimensions      [ 0 0 0 0 0 0 0 ];

internalField   uniform 0;

boundaryField
{
    inlet
    {
        type            fixedValue;
        value           uniform 1;
    }
    "(wind|outlet|sides|base)"
    {
        type            zeroGradient;
    }

}


// ************************************************************************* //
```

Figure A.3: Passive smoke scalar boundary conditions.

```
/*--------------------------------*- C++ -*----------------------------------*\
| =========                 |                                                 |
| \\      /  F ield         | OpenFOAM: The Open Source CFD Toolbox           |
|  \\    /   O peration     | Version:  4.x                                   |
|   \\  /    A nd           | Web:      www.OpenFOAM.org                      |
|    \\/     M anipulation  |                                                 |
\*---------------------------------------------------------------------------*/
FoamFile
{
    version     2.0;
    format      ascii;
    class       volScalarField;
    location    "0";
    object      p;
}
// * * * * * * * * * * * * * * * * * * * * * * * * * * * * * * * * * * * * * //

dimensions      [1 -1 -2 0 0 0 0];

internalField   uniform 91744;

boundaryField
{
    outlet
    {
        type            fixedValue;
        value           $internalField;
    }

    base
    {
        type            calculated;
        value           $internalField;
    }

    inlet
    {
        type            calculated;
        value           $internalField;
    }

    "(wind|sides)"
    {
        type            calculated;
        value           $internalField;
    }
}
```

Figure A.4: Total pressure boundary conditions.

```
/*--------------------------------*- C++ -*----------------------------------*\
| =========                 |                                                 |
| \\      /  F ield         | OpenFOAM: The Open Source CFD Toolbox           |
|  \\    /   O peration     | Version:  4.x                                   |
|   \\  /    A nd           | Web:      www.OpenFOAM.org                      |
|    \\/     M anipulation  |                                                 |
\*---------------------------------------------------------------------------*/
FoamFile
{
    version     2.0;
    format      ascii;
    class       volScalarField;
    location    "0";
    object      p_rgh;
}
// * * * * * * * * * * * * * * * * * * * * * * * * * * * * * * * * * * * * * //

dimensions      [1 -1 -2 0 0 0 0];

internalField   uniform 0;

boundaryField
{
    "(outlet|sides)"
    {
        type            prghTotalHydrostaticPressure;
        p0              $internalField;
        gamma           1;
        value           $internalField;
    }

    base
    {
        type            fixedFluxPressure;
        value           $internalField;
    }

    inlet
    {
        type            fixedFluxPressure;
        value           $internalField;
    }

    wind
    {
        type            fixedFluxPressure;
        value           $internalField;
    }
}


// ************************************************************************* //
```

Figure A.5: p_{rgh} boundary conditions.

```
/*--------------------------------*- C++ -*----------------------------------*\
| =========                 |                                                 |
| \\      /  F ield         | OpenFOAM: The Open Source CFD Toolbox           |
|  \\    /   O peration     | Version:  4.x                                   |
|   \\  /    A nd           | Web:      www.OpenFOAM.org                      |
|    \\/     M anipulation  |                                                 |
\*---------------------------------------------------------------------------*/
FoamFile
{
    version     2.0;
    format      ascii;
    class       volScalarField;
    location    "0";
    object      ph_rgh;
}
// * * * * * * * * * * * * * * * * * * * * * * * * * * * * * * * * * * * * * //

dimensions      [1 -1 -2 0 0 0 0];

internalField   uniform 0;

boundaryField
{
    outlet
    {
        type            fixedValue;
        value           $internalField;
    }

    sides
    {
        type            fixedFluxPressure;
        value           $internalField;
    }

    base
    {
        type            fixedFluxPressure;
        value           $internalField;
    }

    inlet
    {
        type            fixedFluxPressure;
        value           $internalField;
    }

    wind
    {
        type            zeroGradient;
    }
}


// ************************************************************************* //
```

Figure A.6: p_{hrgh} boundary conditions.

```
/*--------------------------------*- C++ -*----------------------------------*\
| =========                 |                                                 |
| \\      /  F ield         | OpenFOAM: The Open Source CFD Toolbox           |
|  \\    /   O peration     | Version:  4.x                                   |
|   \\  /    A nd           | Web:      www.OpenFOAM.org                      |
|    \\/     M anipulation  |                                                 |
\*---------------------------------------------------------------------------*/
FoamFile
{
    version     2.0;
    format      ascii;
    class       volScalarField;
    location    "0";
    object      k;
}
// * * * * * * * * * * * * * * * * * * * * * * * * * * * * * * * * * * * * //

dimensions      [0 2 -2 0 0 0 0];

internalField   uniform 1e-4;

boundaryField
{
    "(outlet|sides)"
    {
        type            inletOutlet;
        inletValue      $internalField;
        value           $internalField;
    }

    base
    {
        type            zeroGradient;
    }

    inlet
    {
        type            fixedValue;
        value           $internalField;
    }

    wind
    {
        type            fixedValue;
        value           $internalField;
    }
}
```

Figure A.7: Turbulent kinetic energy boundary conditions.

```
/*--------------------------------*- C++ -*----------------------------------*\
| =========                 |                                                 |
| \\      /  F ield         | OpenFOAM: The Open Source CFD Toolbox           |
|  \\    /   O peration     | Version:  4.x                                   |
|   \\  /    A nd           | Web:      www.OpenFOAM.org                      |
|    \\/     M anipulation  |                                                 |
\*---------------------------------------------------------------------------*/
FoamFile
{
    version     2.0;
    format      ascii;
    class       volScalarField;
    location    "0";
    object      nut;
}
// * * * * * * * * * * * * * * * * * * * * * * * * * * * * * * * * * * * * * //

dimensions      [0 2 -1 0 0 0 0];

internalField   uniform 0;

boundaryField
{
    "(outlet|sides)"
    {
        type            zeroGradient;
    }

    base
    {
        type            zeroGradient;
    }

    inlet
    {
        type            zeroGradient;
    }

    wind
    {
        type            zeroGradient;
    }
}


// ************************************************************************* //
```

Figure A.8: Turbulent kinematic viscosity boundary conditions.

```
/*--------------------------------*- C++ -*----------------------------------*\
| =========                 |                                                 |
| \\      /  F ield         | OpenFOAM: The Open Source CFD Toolbox           |
|  \\    /   O peration     | Version:  4.x                                   |
|   \\  /    A nd           | Web:      www.OpenFOAM.org                      |
|    \\/     M anipulation  |                                                 |
\*---------------------------------------------------------------------------*/
FoamFile
{
    version     2.0;
    format      ascii;
    class       volScalarField;
    location    "0";
    object      alphat;
}
// * * * * * * * * * * * * * * * * * * * * * * * * * * * * * * * * * * * * * //

dimensions      [1 -1 -1 0 0 0 0];

internalField   uniform 0;

boundaryField
{
    "(outlet|sides)"
    {
        type            zeroGradient;
    }

    base
    {
        type            zeroGradient;
    }

    inlet
    {
        type            zeroGradient;
    }

    wind
    {
        type            zeroGradient;
    }
}


// ************************************************************************* //
```

Figure A.9: Turbulent thermal diffusivity α_T Boundary Conditions.

```
/*--------------------------------*- C++ -*----------------------------------*\
| =========                 |                                                 |
| \\      /  F ield         | OpenFOAM: The Open Source CFD Toolbox           |
|  \\    /   O peration     | Version:  4.x                                   |
|   \\  /    A nd           | Web:      www.OpenFOAM.org                      |
|    \\/     M anipulation  |                                                 |
\*---------------------------------------------------------------------------*/
FoamFile
{
    version     2.0;
    format      ascii;
    class       volScalarField;
    location    "0";
    object      N2;
}
// * * * * * * * * * * * * * * * * * * * * * * * * * * * * * * * * * * * * * //

dimensions      [0 0 0 0 0 0 0];

internalField   uniform 0.76699;

boundaryField
{
    "(outlet|sides)"
    {
        type            inletOutlet;
        inletValue      $internalField;
        value           $internalField;
    }

    base
    {
        type            zeroGradient;
    }

    inlet
    {
        type            fixedValue;
        value           $internalField;
    }

    wind
    {
        type            fixedValue;
        value           $internalField;
    }
}
```

Figure A.10: N_2 specie boundary conditions.

```
/*--------------------------------*- C++ -*----------------------------------*\
| =========                 |                                                 |
| \\      /  F ield         | OpenFOAM: The Open Source CFD Toolbox           |
|  \\    /   O peration     | Version:  4.x                                   |
|   \\  /    A nd           | Web:      www.OpenFOAM.org                      |
|    \\/     M anipulation  |                                                 |
\*---------------------------------------------------------------------------*/
FoamFile
{
    version     2.0;
    format      ascii;
    class       volScalarField;
    location    "0";
    object      O2;
}
// * * * * * * * * * * * * * * * * * * * * * * * * * * * * * * * * * * * * //

dimensions      [0 0 0 0 0 0 0];

internalField   uniform 0.23301;

boundaryField
{
    "(outlet|sides)"
    {
        type            inletOutlet;
        inletValue      $internalField;
        value           $internalField;
    }

    base
    {
        type            zeroGradient;
    }

    inlet
    {
        type            fixedValue;
        value           $internalField;
    }

    wind
    {
        type            fixedValue;
        value           $internalField;
    }
}
```

Figure A.11: O_2 specie boundary conditions.